BULGARIAN ACADEMY OF SCIENCES

INSTITUTE OF OPTICAL MATERIALS AND TECHNOLOGIES
“Acad. Jordan Malinowski”

SYNOPSIS

of the dissertation
for the degree of “doctor of philosophy”

Analysis and compression of dynamic speckle

Mikhail Levchenko

Science specialization
Physics of wave processes

Supervisors:
Prof. DSc Elena Stoykova
Assoc. Prof. Violeta Madjarova, PhD

Sofia, 2024

The dissertation was reviewed and approved for defense at a meeting of the Colloquium of the Institute of Optical Materials and Technologies (IOMT-BAS), held on …………………..
The dissertation consists of a declaration of originality, a list of main symbols and abbreviations, an introduction, 4 chapters, main contributions, a list of the author's publications and presentations referenced in the dissertation, a list of citations of the author's publications and a bibliography of 104 sources in total. The document comprises 142 pages, 134 figures, and 1 table.
The defense of the dissertation will take place on ……………. at ……. in Room ….. of Block 109 of IOMT-BAS in an open session of the scientific jury, composed of:

List of key terms and main abbreviations

ABBREVIATION	MEANING
CMOS	Complementary Metal-Oxide-Semiconductor
C.r.	Compression ratio
DSA	Dynamic speckle analysis
DSI	Dynamic speckle imaging
DSM	Dynamic speckle method
DST	Dynamic speckle technique
FT	Fourier transform
GD	Generalized Differences
GT	Ground truth
IDSM	Intensity-based dynamic speckle method
LASCA	Laser Speckle Contrast Analysis
LSP	Laser speckle photometry
MSF	Modified structure function
MWD	Mean Windowed Difference
NDT	Non-destructive testing
NTCF	Normalized temporal correlation function
PAZO	Poly[1-[4-(3-carboxy-4 hydroxyphenylazo)benzene sulfonamido] -1,2- ethanediyl, sodium salt]
PCA	Principal component analysis
PDF	Probability density function
SF	Structure Function
SSIM	Structural similarity index
SVD	Singular value decomposition
WGD	Weighted generalized differences
WT	Wavelet transform
2D	Two-dimensional

Introduction

Nowadays, there is a pressing demand for the development of robust and effective low-cost optical metrological methods for diagnostics and non-destructive testing. This thesis is dedicated to data analysis and optimization, and image quality enhancement and in dynamic speckle imaging (DSI), a technique based on a speckle phenomenon and representing a wide branch of speckle metrology. The DSI enables monitoring of dynamic events through statistical processing of speckle patterns formed on the surface of a 3D object under laser illumination and captured by a 2D optical sensor. The DSI relies on variation of intensity in the speckle patterns that are due to changes of micro-topography, refractive index or surface parameters caused by some undergoing process in the tested object. Over the years, DSI has developed in two main directions: the application of the method to study different phenomena in specific objects and the elaboration of algorithms for more precise retrieval of the relevant information. The conducted studies in different areas resulted in the establishment of various names for describing the method as “boiling speckle”, “biospeckle”, “dynamic speckle analysis” or “laser speckle photometry”.

The widespread use of DSI is due to all the advantages intrinsic to the coherent optical methods, namely:

1) high sensitivity and spatial resolution;
2) full field measurement;
3) remote sensing and NDT potential;
4) parallel processing of information.

Moreover, when compared to other methods in speckle metrology, the DSI can provide with specific advantages, such as:

1) a single-beam optical scheme leading to simplicity of the optical set-up and higher stability;
2) no requirements for processing the absolute intensity data in a given speckle pattern;
3) low-cost implementation;
4) 2D visualization of information related to the speed of undergoing processes in the studied object at different points in time and space.

Along with these undeniable advantages, the DSI encounters serious issues which may put at risk correct interpretation of the output results. Being an intensity-based approach, the DSI is prone to errors when the laser beam has non-uniform intensity distribution over the object surface. The non-uniformity can lead to a non-related to the observed process changes in the variance of the speckle intensity fluctuations due to the signal-dependent input speckle data. The other serious problem is created by the severe fluctuations of the DSI output data both in space and time due to speckle nature of the input data. These fluctuations decrease substantially the contrast and therefore the sensitivity of the DSI and require statistical processing that must incorporate effective filtering in the temporal and/or spatial domain. Monitoring of processes entails processing of huge amount of data and makes their compression a mandatory step. Moreover, real-time implementations, as well as observation of fast developing processes, require the development of computationally effective algorithms. Outdoor application of DSI relies on the usage of portable set-ups that must be built keeping all necessary restrictions and without providing vibration isolation. At such applications, the DSI is performed under condition of strong environmental noise and its impact on DSI accuracy must be analysed to prove the measurement reliability.

The aim of the thesis is to contribute to the solution of the DSI critical issues by fulfilling the following tasks:

1. Analysis of normalization algorithms in DSI to mitigate the non-uniform laser illumination of the tested object.
2. Analysis of options for temporal resolution improvement of DSI.
3. Analysis of statistical processing at variable in time speckle statistics by using spatial averaging.
4. Analysis of DSI efficiency under outdoor conditions (vibration, ambient light).

5. Development of JPEG-based compression of speckle patterns.
6. Development of Singular value decomposition (SVD)-based compression of speckle patterns.
7. Development of PCA-based compression of speckle patterns with autoencoding.
8. Building a portable smartphone-based DSI set-up.
9. Conducting DSI detection of hidden defects.
10. High-speed camera acquisition and processing of speckle patterns in gas-gun testing of composite materials.

These tasks have been solved by simulating the acquisition of speckle patterns with symmetric/asymmetric intensity distributions and introduced evolution in time, as well as by performing experiments (paint and polymer drying and NDT of samples subjected to low and high-strain rate loading) using four different experimental set-ups and various test object. The obtained results are presented in Chapter 2 (tasks 1-4), Chapter 3 (tasks 5-7) and Chapter 3 (tasks – 8-10). Each of these three chapters ends with a summary. Chapter 1 is dedicated to a literature survey on the historical background, the main areas of applications and the well-established algorithms in the DSI.

Chapter 1 Overview of the dynamic speckle imaging

Speckle is an optical phenomenon which was discovered in 1960s when lasers were developed. Speckle occurs when coherent beam illuminates a rough surface, which leads to interference of scattered light from a sample's surface [1]. As a result, speckle patterns are visible as a random distribution of light and dark spots on the sample. Speckle patterns are characterized by fluctuations of intensity that depend on activity within the sample. There are two types of speckle patterns: a) objective speckle and b) subjective one. Objective speckles refer to speckle patterns observed without the use of an imaging system. Subjective speckle is observed, for instance, when using camera for image acquisition.

Dynamic speckle imaging refers to the temporal fluctuations in speckle patterns that occur when there is an underlying motion or activity within the sample. Such fluctuations are highly sensitive to changes in the object microtopography or refractive index that cause changes in the optical path differences of the interfering light waves.

DSI is based on computational algorithms for estimation of activity within the sample. The speckle patterns, acquired by a CCD or a CMOS camera allows the creation of a 2D spatial distribution of a statistical measure that characterizes the activity in different spatial regions of the sample over a specified time interval [2],[3]. Over the years, numerous point-based statistical estimators have been proposed. Among them are: Fourier transform(FT)[4]; Wavelet transform (WT)[4], which convert signal into the time-frequency domain; Fujii's method [5], which processes biospeckle images; Generalized Differences (GD) [6] algorithm which is applied for uniformly as well as non-uniformly illuminated samples; Mean Windowed Difference (MWD) [7] increasing the sensitivity of algorithm; Structure Function (SF) [8] algorithm, for uniform distribution of intensity fluctuation along the object; and Modified Structure Function (MSF) [9] algorithm. In our research we mostly used two algorithms: SF and MSF. The main reason is that both work faster than GD, MWD and their modifications, while being highly sensitive to activity changes.

SF, maintains sensitivity and provides faster computation time. For a temporal lag $\tau = m\,\Delta t$, the temporal SF is mathematically defined as:

$$SF(i,k) = \sum_{j=1}^{N-m} \left[I_{ik,j} - I_{ik,j+m}\right]^2 \tag{1.1}$$

MSF was introduced as an alternative to the SF technique by substituting the squared term with the absolute value of the difference $\left|I_{ik,j} - I_{ik,j+m}\right|$. The estimate is calculated as follows:

$$MSF(i,k) = \sum_{j=1}^{N-m} \left|I_{ik,j} - I_{ik,j+m}\right| \tag{1.2}$$

where $m = 1,2 \ldots M, M < N$ and j is the index covering the range of registered images.

DSI technique is used in numerous different fields. For example, in biomedical imaging, dynamic speckle patterns have been used to study blood flow [10-13], penetration of cosmetic ingredients in human skin [14], ear biometrics [15], bacterial response [16-17], plants growth and leaves chemical contamination [18-19], seeds viability [20], animal reproduction [21]. In industrial applications DSI is used for food quality assessment [22-24], drying of paints, coatings and polymer thin films [25-26] and for defect detection within such materials as metals [27-28], ceramics [29], polymers and composites [30-31].

Chapter 2 Analysis of Dynamic speckle imaging

The studies in the Second Chapter refer to author's papers A1-A5.

2.1 Normalization in dynamic speckle analysis

2.1.1 Normalized processing

As a first task, we focused on analysing normalization techniques for processing data with spatially varying speckle statistics, such as those acquired under non-uniform illumination. Our research is based on the conventional optical setup with a sample on vibration isolated table, a laser source, a 2D optical sensor and computer for capturing and processing of speckle pattern images as illustrated in Figure 1.

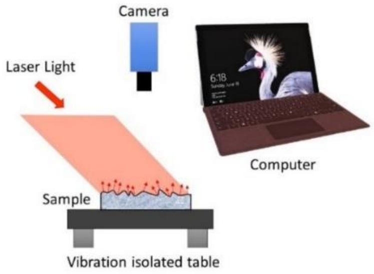

Figure 1 Experimental setup for capturing speckle pattern images

The pointwise processing of the 2D speckle images is depicted in Figure 2 . To construct an activity map of the sample, a sequence of N time-correlated speckle pattern images is used, with a time interval between successive images equal to Δt.

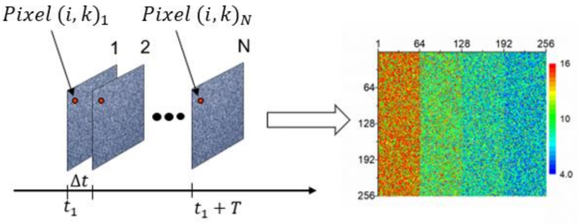

Figure 2 Building an activity map by acquiring a set of time-correlated speckle images and applying the modified structure function algorithm

The activity estimate is calculated by averaging over the time interval, $T = N\Delta t$. The temporal correlation function $R_{ik}(\tau)$, where $\tau = m\Delta t$ is the time lag between the compared intensities and $m \geq 0$ is an integer, characterizes intensity fluctuations at pixel $(i\Delta, k\Delta)$. The width of $R_{ik}(\tau)$ determines the temporal correlation radius $\tau_c(i\Delta, k\Delta)$. Under non-uniform illumination, the variance of intensity fluctuations, σ_{ik}^2 , in $R_{ik}(\tau) = \sigma_{ik}^2 \rho_{ik}(\tau)$ varies from point to point, where $\rho_{ik}(\tau)$ is the normalized correlation function. Due to the signal-dependent nature of speckle intensity fluctuations, normalized processing may be required.

To evaluate the performance of different normalization algorithms, we generated speckle patterns for a synthetic object composed of four rectangular regions Z_1, Z_2, Z_3 and Z_4, all of equal size but with temporal correlation radii of intensity fluctuations equal to $10\Delta t$, $20\Delta t$, $40\Delta t$, and $80\Delta t$ respectively (Figure 3 a). The simulation involved generating correlated wrapped phase distributions in the object plane, which were then propagated to the sensor plane through an objective lens using a scalar diffraction theory. A 2D array of random delta-correlated phase values, uniformly distributed from 0 to 2π, was used as the initial phase. A normal distribution was assumed for phase changes over time, reflecting the movement of scattering centres relative to the surface. The amplitudes and phases of scattered light at each scattering centre and between centres were assumed to be mutually independent. We used $\rho_{ik}(\tau) = \exp\left\{-\frac{\tau}{\tau_c(i\Delta, k\Delta)}\right\}$ to describe the modeled processes.

The standard deviation of the phase change between successive images was $\sigma_{\phi} = N(0,1)[\frac{\Delta t}{\tau_c(i\Delta,k\Delta)}]^{1/2}$, where $N(0,1)$ denotes a random variable characterized by normal distribution with a zero mean and a standard deviation equal to 1. The integration of speckle by camera pixels was also considered.

Speckle patterns of 256×256 pixels were generated for both low and high contrast speckle at a wavelength of 532 nm under both uniform and non-uniform illumination. A Gaussian intensity distribution $I_0(i\Delta, k\Delta) = I_0 \exp\{-\alpha(i\Delta, k\Delta)\}$, where $I_0 = \text{const}$ and $\alpha(i\Delta, k\Delta) = \frac{(i-128)^2\Delta^2+(k-128)^2\Delta^2}{\Omega^2}$ with $\Omega = 210\Delta$ was used for the simulation. The histograms of intensity fluctuations across the object and the speckle patterns for the four simulated cases are shown in Figure 3 (b) and Figure 3(c).

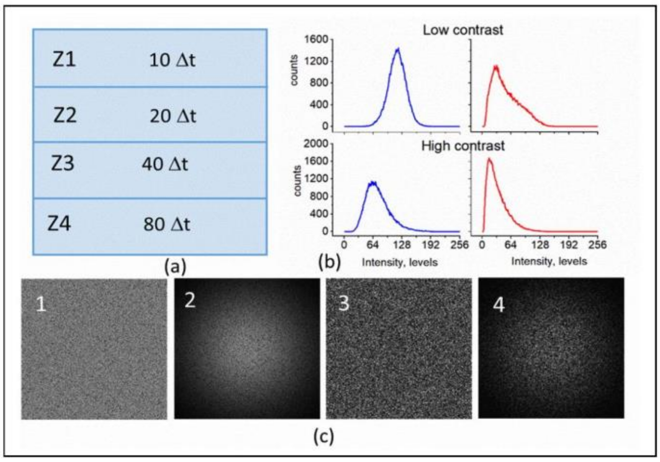

Figure 3 Synthetic object with four activity regions $\mathrm{Z}_1, \mathrm{Z}_2, \mathrm{Z}_3$, and Z_4 with temporal correlation radii of intensity fluctuations equal to 10Δt, 20Δt, 40Δt, and 80Δt (a), speckle intensity histograms (b) for patterns (c) obtained for the object at low contrast and uniform (1) and non-uniform (2) illumination and high contrast and uniform (3) and non-uniform (4) illumination; wavelength 532nm, image size 256×256 pixels.

Under uniform illumination, speckle statistics is the same across regions $\mathrm{Z}_1, \mathrm{Z}_2, \mathrm{Z}_3$ and Z_4, characterized by symmetric or asymmetric intensity distributions depending on the speckle contrast. In areas of higher or lower activity, speckle exhibits similar statistics, requiring time-averaging to visualize these regions. Under non-uniform illumination, the intensity histograms in the acquired patterns become asymmetric for both low and high contrast due to darker regions in the captured images.

Evaluation of activity is provided by the normalized estimates of the structure function S_1 and the modified structure function S_2:

$$S_{norm}(i,k,m) = \frac{1}{(N-m)v_{ik}} \sum_{n=1}^{N-m} \left(I_{ik,n} - I_{ik,n+m}\right)^2 \tag{2.1}$$

$$S_2(i,k,m) = \frac{1}{N v_{ik}^{1/2}} \sum_{n=1}^{N-m} \left|I_{ik,n+m} - I_{ik,n}\right| \tag{2.2}$$

where $v_{ik} = \frac{1}{N}\sum_{n=1}^{N}(I_{ik,n} - I_{ik})^2$, N is the number of speckle images, $m = 1,2\ldots M, M < N$ is the time lag in units of Δt and (i,k) correspond to coordinates of pixels, $I_{ik,n}$is the intensity value.

Pointwise evaluation of the average value and the variance from the intensity sequences at all pixels complicates these algorithms. The computation of variance v_{ik} by averaging over time is reliable when the ratio of acquisition time $T = N\Delta t$ to the temporal correlation radius τ_c is relatively high. Instead of using v_{ik}, one might use the average intensity value or its square for normalization. More flexible algorithms can be developed by time-averaging fractions where the numerator and denominator are composed of one or two intensity values acquired at different times. We evaluated several estimates: $S_l(i,k,m) = \frac{1}{N-m}\sum_{n=1}^{N-m} f_{ik,n}^{l}(m)$, with $f_{ik,n}^{3}(m) = \frac{I_{ik,n}}{I_{ik,n+m}}$, $f_{ik,n}^{4}(m) = \left|\frac{I_{ik,n}}{I_{ik,n+m}} - 1\right|$, $f_{ik,n}^{5}(m) = \left|\frac{I_{ik,n}-I_{ik,n+2m}}{I_{ik,n+m}}\right|$, $f_{ik,n}^{6}(m) = \frac{|I_{ik,n}-I_{ik,n+m}|}{I_{ik,n}+I_{ik,n+m}}$, $f_{ik,n}^{7}(m) = \left|\frac{I_{ik,n}}{I_{ik,n+m}} - \frac{I_{ik,n+m}}{I_{ik,n}}\right|$

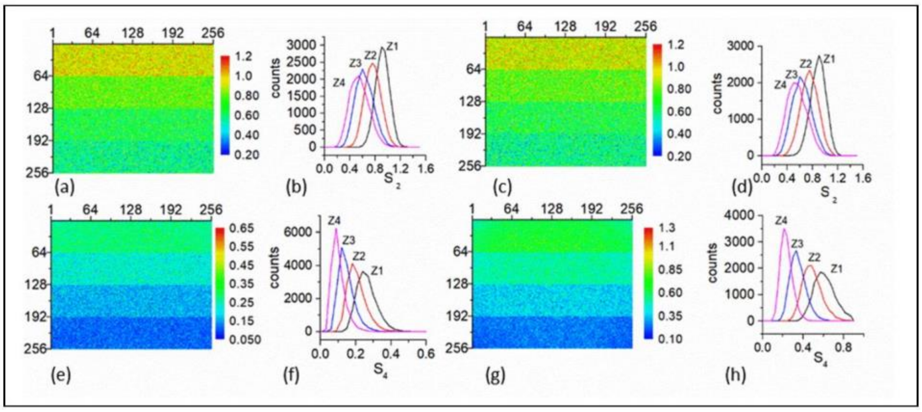

Figure 4 Activity maps for the synthetic object with 4 activity regions $\mathrm{Z}_1, \mathrm{Z}_2, \mathrm{Z}_3, \mathrm{Z}_4$ (a, c, e, g) and the histograms of the estimates in these regions (b, d, f, h) for estimates S_2 (a, b, c, d) and S_4 (e, f, g, h); (a, b, e, f) - low contrast speckle, (c, d, g, h) - high contrast speckle. $\mathrm{N} = 256$, wavelength = 532 nm, $\mathrm{m} = 10$.

Figure 4 presents activity maps obtained for S_2 and S_4. The four regions of varying activity are clearly visible for both estimates. The map corresponding to S_4 appears to have better contrast, especially for regions Z_3 and Z_4 with lower activity.

2.1.2 Processing of experimental data

For the experimental validation of the algorithms, we used a specially designed circular metal object with flat annular regions of alternating depths (0 mm and -2 mm) relative to the upper surface. This object features two flat regions at zero depth and two hollow regions: a central circular section and an annular region. Different levels of surface activity were created by applying a polyester paint that formed a flat layer over the object. The hollow regions thus accumulated more paint compared to the flat surface areas of the other two annular regions. The object was placed on a vibration-insulated table and illuminated with linearly polarized light from a He-Ne laser at 632.8 nm. The paint drying process produced dynamic speckle, and the speckle patterns were captured as 8-bit bitmap images using a colour CMOS camera X06c-s (Baumer Ltd) with a frame interval of $\Delta t = 250$ ms. Each image had a resolution of 780 × 582 pixels, a file size of 1.29 MB, and an exposure time of 100 µs. An example of a speckle image in bitmap format is shown in Figure 5(a). As illustrated, the intensity distribution across the image is non-uniform, making it challenging to distinguish between regions of different activity. We compared the performance of normalized processing using S_1, S_2 and S_4. The maps of these estimates, processed from 256 patterns with a time lag of $10\Delta t$, are presented in Figure 5 (b-d).

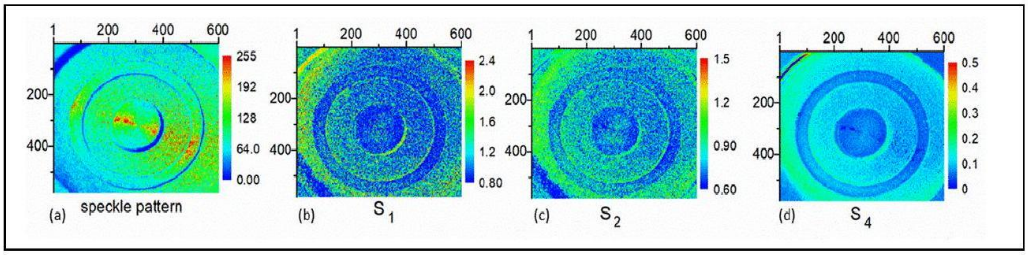

Figure 5 Speckle pattern acquired for a circular metal object with annular regions of different depths in a bitmap format (a) and activity maps for S_1 (b), S_2 (c), and S_4 (d); $N = 256$, wavelength 632.8 nm, $m = 10$

Despite the relatively long image sequence, the estimate v_{ik} introduces additional fluctuations in S_1 and S_2, which affects the sensitivity of these estimators. Non-normalized structure and modified structure functions produce smoother maps but with less accurate activity determination due to illumination non-uniformity. The S_4 algorithm provides an activity map with an improved contrast. Next, we studied influence of acquisition time of speckle images on quality of calculated activity maps.

2.2 Temporal resolution improvement in dynamic speckle analysis

The selection of the time interval Δt is specific to the task and is associated with the temporal correlation radius τ_c of the intensity fluctuations resulting from the monitored process. Therefore, determining the optimal acquisition time, T, of speckle images is crucial in achieving a balance between reasonable temporal resolution and high-quality activity maps.

2.2.1 Impact of the ratio between the temporal correlation radius and the sampling step in time

The test object again consisted of four rectangular areas with different constant activities given by the correlation radii in time, $\tau_{c1}, \tau_{c2}, \tau_{c3}, \tau_{c4}$. Each region is 64 x 256 pixels in size. Activity maps were created by applying the MSF algorithm to 256 simulated speckle images, with an acquisition time $T = 256\Delta t$. In the first iteration, Δt was set equal to τ_c of the fastest process, with values $\tau_{c1} = \Delta t$, $\tau_{c2} = 2\Delta t$, $\tau_{c3} = 3\Delta t$, $\tau_{c4} = 4\Delta t$. In the second iteration, Δt was set less than all τ_c as follows: $\tau_{c1} = 10\Delta t, \tau_{c2} = 20\Delta t, \tau_{c3} = 30\Delta t, \tau_{c4} = 40\Delta t$. Finally, in the last test, Δt was much smaller than τ_c, with values $\tau_{c1} = 100\Delta t; \tau_{c2} = 200\Delta t; \tau_{c3} = 300\Delta t; \tau_{c4} = 400\Delta t$. The activity maps from all three iterations are shown in Figure 6 (b, d, f), with corresponding activity estimate histograms in Figure 6 (a, c, e).

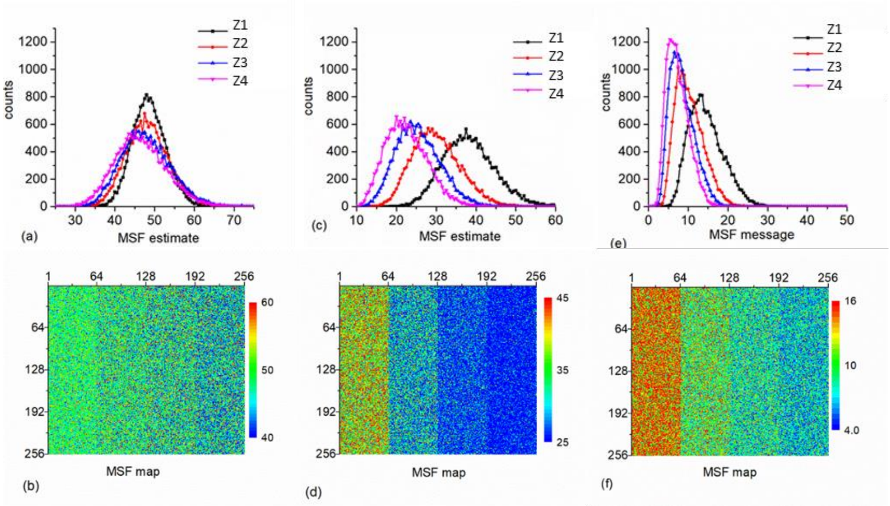

Figure 6 Built activity maps: (b) Δt is equal to τ_{c1}; (d) Δt is less than τ_{c1-4}; (f) Δt is much less than τ_{c1-4} and their histograms of MSF estimate (a, c, e)

It can be seen that the decreasing of the time interval between the speckle images increases the sensitivity and contrast of the MSF algorithm.

Next, the impact of time resolution on the quality of the activity maps was examined by generating 1024 speckle pattern images of the same object with four rectangular regions with different activity. The activity values of the simulated sample were : $\tau_{c1} = 40\delta t$; $\tau_{c2} = 80\delta t$; $\tau_{c3} = 160\delta t$; $\tau_{c4} = 320\delta t$, where δt is the time interval used for generation of the speckle patterns. As is seen, it is rather small compared to the activity values. Using these patterns, three synthetic experiments have been carried out with $N = 256$ at $\Delta t = \alpha\delta t$ for α being an integer equal to 1, 2 and 4 to build the activity maps and the histograms as the estimates of the probability density functions (PDFs) of activity estimates corresponding to decreasing acquisition time. The activity maps are shown in Figure 7(b, d, f), with the corresponding PDFs in Figure 7(a, c, e).

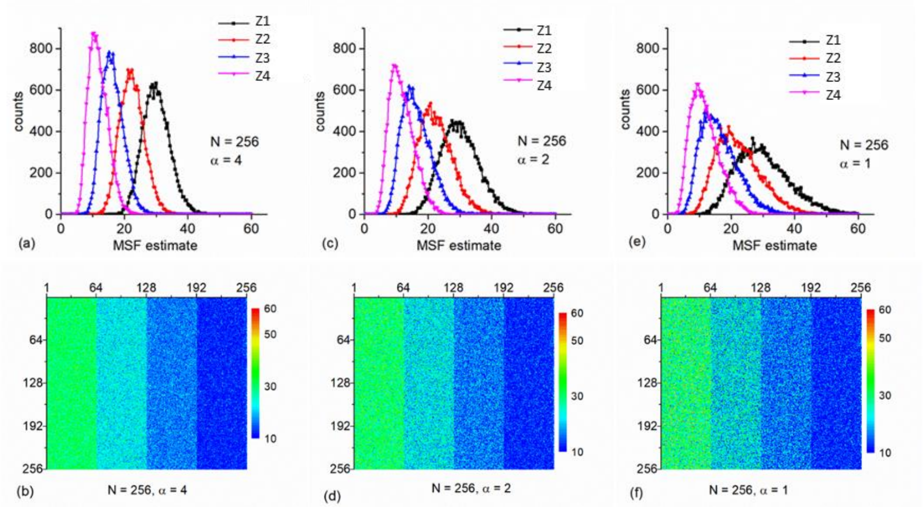

Figure 7 Built activity maps: (b) α $= 4$; $T = T_1$; (d) α $= 2$, $T = T_1/2$; (f) α $= 1$, temporal resolution $T = T_1/4$. PDFs (a), (c), (e) from left to right relatively to activity maps.

The contrast of all images makes it easy to distinguish between different activity areas. As expected, increasing time resolution by decreasing the acquisition time also increases intensity fluctuations, as evidenced by the histograms.

2.2.2 Polymer drying experiment

An experiment involving a drying polymer was conducted to validate the results obtained from the simulation experiments. In this study, 40 mg of the azopolymer Poly[1-[4-(3-carboxy-4 hydroxyphenylazo)benzene sulfonamido] -1,2- ethanediyl, sodium salt] (PAZO) was dissolved in 400 µL of water, and a 100 µL droplet was spread on a glass substrate.

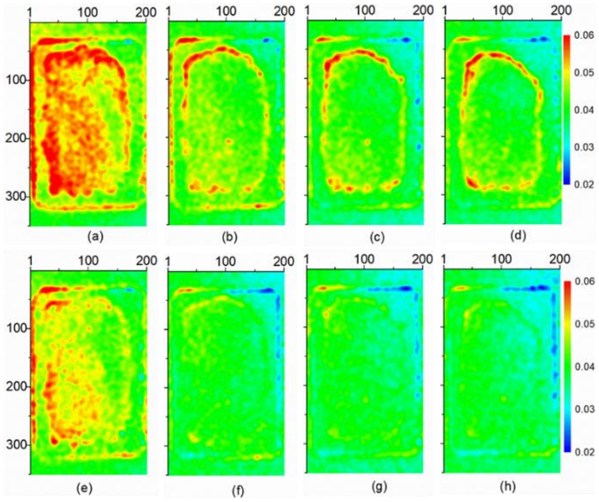

Figure 8 Computed activity maps from left to right, recorded at the time offsets t = 0, 2, 4 and 6 min from the start of the experiment. Upper row - Δt_2 =1 s. Lower row - Δt_1 = 250 ms.

The resulting activity maps display better contrast with the time resolution $T_2 = N$ x $\Delta t_2 = 64$ s. The polymer drying process is observable at each time interval, with changes in activity particularly noticeable at the edges of the PAZO layer. Despite some difficulties, it is still possible to discern activity processes within the polymer even when the time resolution is increased fourfold (lower row). Thus, the experiment with the polymer confirms the results obtained in the simulated tests. It is practically proven that even with increased time resolution, it is still possible to distinguish activity maps recorded at different time instants.

2.3 Dynamic speckle method for analysis of variable-rate dynamic events

A pointwise estimate provides reliable maps for symmetrical/asymmetrical speckle intensity distributions. The 2D map estimate is non-linearly related to the spatial distribution of the temporal correlation radius $\tau_c(i,k)$ of intensity fluctuations on the object surface. A decrease of $\tau_c(i,k)$ indicates increased activity. The activity estimates analyzed in the previous sections are obtained by averaging over time, with spatial resolution determined by the pixel pitch. However, this advantage is somewhat compromised because the estimate can fluctuate significantly from point to point, reducing the map contrast. A high-contrast map entails a narrow PDF or histogram of the chosen estimate at a given τ_c. The spread of this histogram decreases with the averaging interval $T = N\Delta t$, which can be either greater than or less than $\tau_c(i,k)$ at different points on the object. The estimates in the previous sections assume that $\tau_c(i,k)$ remains constant during the capture of the required N images.

We consider the scenario where the temporal correlation radius also depends on time, such that $\tau_c = \tau_c(x,y,t)$. Specifically, we assume the acquisition rate is comparable to the rate of change of τ_c, meaning that each new captured image at $t = n\Delta t$ corresponds to a new spatial distribution $\tau_c(x,y,t = n\Delta t)$. Again, we support our analysis by conducting synthetic and real experiments.

2.3.1 Analysis of variable-rate dynamic events

For analysis of variable-rate dynamic events, we generated 256 speckle patterns using the following model for the temporal correlation radius:

$$\tau_c(i,k,n) = 260\varDelta t - (n-1)\varDelta t \times exp(-\frac{(i\varDelta - 128\varDelta)^2 + (k\varDelta - 128\varDelta)^2}{(112\varDelta)^2}) \qquad (2.3)$$

Where $n = 1, 2, \ldots, 256$. The object is illuminated by an expanded laser beam with a uniform intensity distribution at wavelength λ. It's sufficient to assume that the scattering centres move randomly in directions normal to the surface. The complex amplitudes of light scattered from these centres have mutually independent amplitudes and phases, both for a given centre and between different centres, with no temporal change in reflectivity observed across the object during data acquisition. Thus, the phase change due to height variation of a scattering center is normally distributed at each point.

The phase change $\Delta\phi_m^{ik,n}$ at point $(i\Delta, k\Delta)$ between moments $n\Delta t$ and $(n+m)\Delta t$, separated by a time lag $\tau = m\Delta t$, leads to intensity fluctuations in the optical sensor, with a normalized correlation function given by: $\rho_{ik,n}(m\Delta t) = \exp\left(-\sigma^2_{\Delta\phi_m^{ik,n}}\right)$, where $\sigma^2_{\Delta\,\phi_m^{ik,n}}$ is the variance of the phase change. We used the model: $\rho_{ik,n}(\tau) = \exp\left(-\frac{\tau}{\tau_c(i,k,n\Delta t)}\right)$. As has been mentioned before, this model effectively describes various processes, such as e.g. drying. We assume that the following formula is applicable for the standard deviation of the phase change for images $(n-1)$ and n: $\sigma_{\Delta\phi_{ik,n}} = \sqrt{\frac{\Delta t}{\tau_c(i,k,n\Delta t)}}$, where $n\Delta t$ is the time of recording the nth image.

For the simulation, delta-correlated random phases $\phi(i\delta, k\delta, n\Delta t)$ for $i = 1..2N_x$, $k = 1..2N_y$, and $n = 1..N$ were generated on the object surface at a spatial step $\delta = \Delta/2$, starting from a 2D array of phase values uniformly distributed from 0 to 2π. The phase distribution at time $n\Delta t$ for $n \geq 2$ is found from: $\phi(i,k,n\Delta t) = \phi(i,k,(n-1)\Delta t) + \chi_{ik,n}\sqrt{\frac{\Delta t}{\tau_c(i,k,n\Delta t)}}$, where $\chi_{ik,n}$ is a random number with a standard normal distribution (mean 0, variance 1), separately generated for each i, k, n. The complex amplitude on the object surface was generated from $\phi(i\delta, k\delta, n\Delta t)$ for the laser beam's intensity distribution $I_0(i\delta, k\delta)$ as $U_S = I_0(i\delta, k\delta)\exp\big(-j\phi(i\delta, k\delta, n\Delta t)\big)$, where j is the imaginary unit. The spatial intensity distribution $I_0(i\delta, k\delta)$ of the laser beam was given by real numbers. The complex amplitude of the light field on the sensor aperture was then generated as: $U_{\mathrm{cam}} = \mathrm{FT}^{-1}\big\{H \cdot \mathrm{FT}\{U_S\}\big\}$, where $\mathrm{FT}\{\cdot\}$ denotes the Fourier transform, and H is a circ function in the Fourier domain with a cut-off frequency equal to $\frac{N_x D}{2\lambda f}$, where D and f are the diameter and focal distance of the camera objective, respectively. It was assumed that $N_x = N_y$. Speckle integration by the camera pixels was done by summing the values of $|U_{\mathrm{cam}}|^2$ within a 2×2 pixel window. The exposure interval was much shorter than Δt, so no averaging of the speckle pattern within this interval was simulated. Figure 9(a) shows the spatial distribution of $\tau_c(x, y, t = 240\Delta t)$.

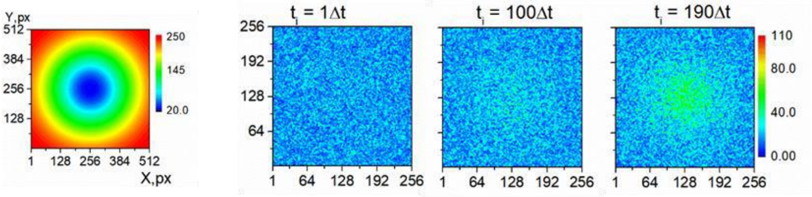

(a) (b)

Figure 9 Spatial distribution of the temporal correlation radius for the model given by formula (2.3) at the instant $t = 240\ \Delta t$ (a); activity maps of MSF estimate corresponding to different initial instants in the processed sequences of intensity; time lag $\tau = 15\ \Delta t$. The image size is 256 × 256 pixels, with uniform illumination at 532 nm (b).

The pointwise processing with temporal averaging fails to provide adequate activity maps for the model (2.3). To improve the evaluation of activity in such fast-developing processes, averaging should be performed in the spatial domain. This can be done by dividing each image into equal-sized segments that slide by one pixel within the image and calculating the estimate for a specific time lag using only two images, averaging within each segment:

$$S_3(i,k,n,m) = \frac{1}{ss^2} \sum_{v=i-ss/2}^{i+ss/2} \sum_{j=k-ss/2}^{k+ss/2} \left| I_{vj,n} - I_{vj,n+m} \right| \qquad (2.4)$$

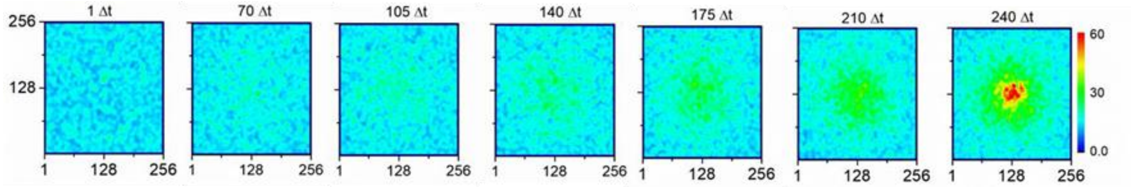

Figure 10 Activity maps for estimate (2.4) at different moments for the model given by Equation (2.3) and a time lag $\tau = 15\ \Delta t$; image size is 256 × 256 pixels, segment size 8 × 8 pixels, uniform illumination at 532 nm

2.3.2 Experimental check

To validate the developed approach, we recorded a sequence of speckle images during the drying of a polymer solution. The polymer used was PAZO. The methanol droplet dried completely in under 2 minutes at 30°C. The glass slide was placed on a hot stage (THMS 600 from Linkam Scientific) which maintained the sample at a set temperature. Thermal equilibrium was ensured by allowing the glass substrate to sit on the stage for 5 minutes at the desired temperature before applying the droplet. The temperatures used were 30°C, 40°C, and 50°C. The exposure time was 20 microseconds, and the interval Δt between consecutive images was 250 milliseconds. Room temperature was maintained at 25°C throughout the experiment, monitored by an air-conditioning system.

The activity maps in Figure 11 show a decrease in activity over time: the highest activity occurs at the start of drying and decreases to nearly zero. The decrease in activity is slowest at 30°C. The maps are plotted using the same colour scale for easier comparison.

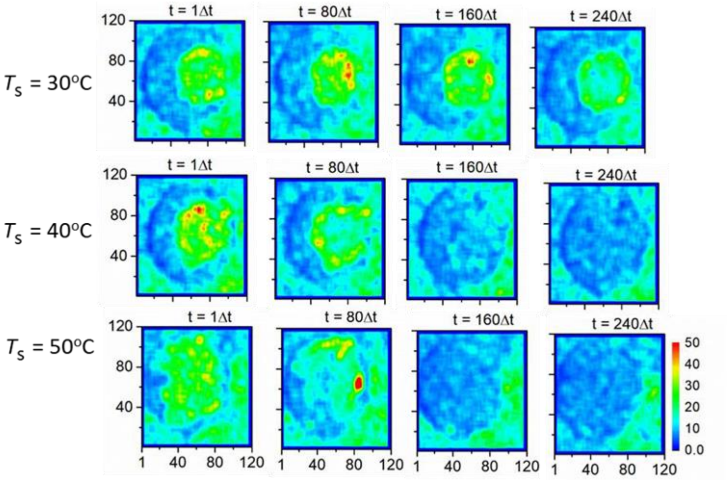

Figure 11 Activity maps for estimate (2.4) at different instants and temperatures during the polymer droplet drying experiment, with a time lag of $\tau = 10\Delta t$. The image size is 120 × 120 pixels, segment size is 8 × 8 pixels, and the illumination wavelength is 632.8 nm.

2.4 Noise analysis in outdoor dynamic speckle measurement

For industrial or medical applications, DSI-based non-destructive testing must be effective under outdoor conditions. This involves data acquisition in environments with increased phase noise due to the absence of vibration isolation and the presence of ambient light.

2.4.1. Noise analysis of synthetic speckle images

We described simulation process in the Section 2.3.1, therefore only noise simulation is described here.

The environmental phase noise was introduced at each time instant, $i\Delta n$, where $i = n \ldots N$ starting from $n \geq 2$. We assumed that the noisy fluctuations followed the same probability distribution at every moment and shared the same temporal correlation length, τ_{noise}. Similarly to the phase change associated with the observed process, we assumed the standard deviation of the environmental phase fluctuations was given by $\sigma_{noise} = \alpha\sqrt{\Delta t/\tau_{noise}}$, where the parameter α is less than 1. This parameter α was introduced to account for the fact that the magnitude of the noisy fluctuations is expected to be smaller than the phase change caused by the observed process.

The complex amplitude on the object's surface was derived from the phase distributions $\phi(i\delta, k\delta, n\Delta t)$ with added phase noise, corresponding to the intensity distribution $I_0(i\delta, k\delta)$ of the laser beam on the object's surface at time $n\Delta t$. It was expressed as $U_S = \sqrt{I_0(i\delta, k\delta)} exp\,\{-j[\phi(i\delta, k\delta, n\Delta t) + \theta_{ik,n}\sigma_{noise}]\}$, where j is the imaginary unit and $\theta_{ik,n}$ is a random variable drawn from a standard normal distribution with zero mean and unit variance. This random variable $\theta_{ik,n}$ was generated separately for each combination of indices i, k and n. At this point in the simulation, it is important to note that the spatial intensity distribution $I_0(i\delta, k\delta)$ of the laser beam was not constrained to integer values.

We also described simulation of the integration of speckle by the camera pixels in Section 2.3.1, which means that description of shot noise from laser photons and quantization noise from encoding the signal as 8-bit images only left. These two types of noise are the most substantial at acquisition and inevitably exist in all raw data, even in those captured in a darkened environment with vibration isolation.

At outdoor capture, ambient light enters the sensor aperture, and the photons at wavelengths within the curve of spectral sensitivity of the camera create additional shot noise. Therefore, the detection was simulated at assumptions that (1) the average number of signal photons arriving within the exposure interval with energy corresponding to the laser wavelength was $N_{ph}(i, k)$, (2) the maximum average number of signal photons within the exposure interval for the acquired images was N_{max}, and (3) ambient light created an equivalent average number of photons, $N_{al} = \eta N_{max}$, which was the same for all pixels. We assumed for the simulation that parameter η was less than 1. The shot noise was modelled as a random number with a Poisson distribution with average and variance equal to N_{ph} $(i,\ k)$ + N_{al}. To determine N_{ph} $(i,\ k)$, the maximum intensity in the generated 2D speckle intensity distributions before the procedure of quantization was taken to correspond to N_{max}. The camera dynamic range was adjusted to cover a signal equivalent to $N_{max}+\sqrt{N_{max}}$. The simulated raw data were transformed to 8-bit encoded bitmap images for further processing.

We applied non-normalized MSF to simulated speckle images with noise:

$$S_1(i,k) = \sum_{j=1}^{N-m} \left| I_{ik,j} - I_{ik,j+m} \right| \tag{2.5}$$

and normalized one:

$$S_2(i,k) = \frac{1}{N} \sum_{n=1}^{N-m} \frac{|\ I_{ik,n} - I_{ik,n+m}\ |}{I_{ik,n} + I_{ik,n+m}} \tag{2.6}$$

Estimate S_1 is only slightly affected by the shot noise from ambient light. For the S_2, the impact of ambient light is much stronger due to its effect on the denominator.

The results of simulation at constant activity when the temporal correlation radius is the same across the object suggest that a normalized estimate with low sensitivity to ambient light shot noise is needed. We propose estimate 3:

$$S_3(i,k,m) = \frac{1}{N-m} \sum_{n=1}^{N-m} \frac{\left| I_{ik,n} - I_{ik,n+m} \right|}{\sigma_{ik}} \tag{2.7}$$

where the standard deviation σ_{ik} is given by $\sigma_{ik}^2 = \frac{1}{N}\sum_{n=1}^{N}\left(I_{ik,n} - \overline{I_{ik}}\right)^2$, $\overline{I_{ik}} = \frac{1}{N}\sum_{n=1}^{N} I_{ik,n}$.

Next, we investigated the contrast of activity maps obtained in a noisy environment for a test object with two distinct activity levels and clear borders between these areas. The high-activity areas were shaped by the logos "IOMT" and "ETRI" of the home institution and the partner institution respectively involved in the PLENOPTIMA project.

The contrast and sensitivity of activity maps under Gaussian illumination for estimates S_2 and S_3 are presented in Figure 12. The obtained in the absence of noise ground truth (GT) maps are compared to those derived from data with only phase noise and those with both phase noise and ambient light. Estimate S_2 fails to accurately reconstruct activity under Gaussian illumination and ambient light, showing a significant shift to lower activity values and a decrease in activity from the centre to the edges of the map. In contrast, estimate S_3 correctly captures activity variation, but the contrast of the maps is relatively low.

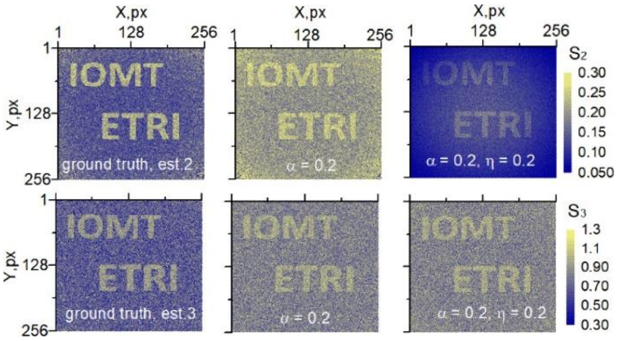

Figure 12 Activity maps of estimate S_2 (top) and estimate S_3 (bottom) for an object with two activity levels (two logos and background) for Gaussian illumination at phase noise and ambient light shot noise: τ_{noise} = Δt, τ_{cl} = 10Δt, τ_{cb}= 50Δt, N = 200

We introduced a contrast parameter $\beta = (S_l - S_b)/S_l$ to evaluate the quality of the activity map, where S_l and S_b are the mean values of the estimate in the logo areas and the background, respectively. This parameter was used to study the impact of environmental phase noise with a correlation radius τ_{noise}. Results for estimate S_1 show that as τ_{noise} increases, the contrast improves, approaching the GT map's value (Figure 13).

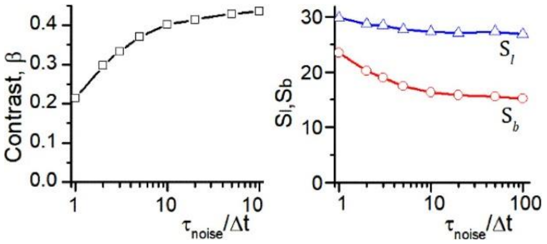

Figure 13 Contrast parameter, β, for activity maps of estimate S_1 (left) and mean activity values in the high activity area (S_l) and low activity area (S_b) as a function of the correlation radius of the phase noise: τ_{noise} = Δt, τ_{cl} = 10Δt, τ_{cb}= 50Δt, *N* = 200, uniform illumination.

2.4.2 Experimental noise analysis

We conducted an experiment with a test object placed on a vibration-isolated table, illuminated by a beam of linearly polarized laser light at 632.8 nm wavelength. The laser power density, measured with a THORLABS PM100D power meter, was 0.67 mW/cm² on the object's surface. A Basler acA4096-30um camera, with a resolution of 4096 px × 2168 px, pixel pitch of 3.45 µm, and an exposure time of 20 ms, captured speckle images. Speckle images were taken at $\Delta t = 2$ s, and a laptop computer was used for setting recording parameters and storing the raw images. The test object contained the logos "IOMT" and "ETRI" created as hollow regions on the object. Both the hollow regions and the flat surface were covered with Tamiya Mini X-2 White acrylic paint to ensure a smooth layer, applied with a brush. We performed two sets of experiments: one with ambient light and one without, with vibration isolation turned on. We recorded two series of 1200 images for each case, with the object being repainted twice. The time series was divided into six sets of 200 images each. The activity maps for these sets, with and without ambient light, are displayed in Figure 14 and Figure 15. The coordinates on the maps are in pixels. Due to slight illumination non-uniformity, estimate S_2 was used for processing with a time lag of $\Delta t = 51$ s.

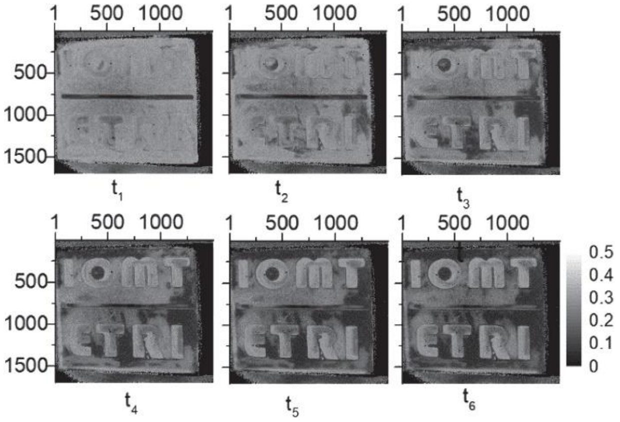

Figure 14 Activity maps of estimate S_2 for a covered with paint 3D object with a flat surface and hollow regions in a darkened room and vibration isolation turned on; t_1 = 0 s ; t_2 = 6 min 40 s ; t_3 = 13 min 20 s, ; t_4 = 20 min, ; t_5 = 26 min 40 s, ; t_6 = 33 min 20 s, *N* = 200, τ = 5*Δ*t. The coordinates along the horizontal and vertical axes of the maps are in pixels.

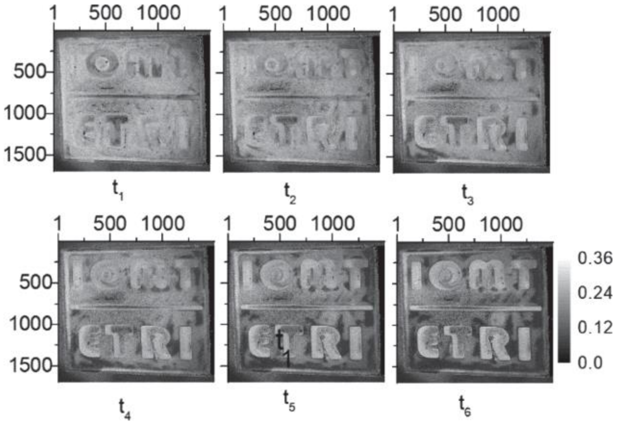

Figure 15 Activity maps of estimate S_2 for a covered with paint 3D object with a flat surface and hollow regions in the presence of ambient light and vibration isolation turned on; t_1 = 0 s ; t_2 = 6 min 40 s ; t_3 = 13 min 20 s, ; t_4 = 20 min, ; t_5 = 26 min 40 s, ; t_6 = 33 min 20 s, N = 200, τ = 5Δt. The coordinates along the horizontal and vertical axes of the maps are in pixels.

Both cases showed similar behavior: maps transitioned from showing more uniformly distributed high activity at the start to higher activity concentrated in the letter regions by the end of the experiment. The non-uniformity in the background likely resulted from uneven paint application with the brush. As expected, the average value of estimate S_2 was lower with ambient light due to increased shot noise, confirming that drying can be reliably monitored even with ambient light present.

Chapter 3 Compression of dynamic speckle images

The studies in the Third Chapter refer to author's papers A6, A7.

3.1 JPEG and JPEG2000 compression in intensity-based dynamic speckle analysis (DSA)

A sequence of speckle images is required for a single activity map at pointwise processing. Considerable number of maps, in its turn, is required to analyse evolution of a process in time. This means that big amount of data should be stored on a disk space for DSA. Data compression becomes a mandatory step for the DSA implementation. The goal of the conducted study is to demonstrate that images compressed using JPEG or JPEG2000 are suitable for pointwise DSA.

3.1.1 Distortions in activity maps from decompressed speckle images

DSA identifies areas with different speed of processes. For the synthetic experiment, we simulated an object with two distinct regions of rapid activity, embedded in a background with slower intensity changes. High-activity regions are the logos "IOMT" and "ETRI". The simulation parameters were as follows: temporal correlation radii for the logos and the background were τ_{cl}= 10Δ and τ_{cb} = 40Δ, respectively; time lag τ = 10Δt (m = 10); image size 256×256 pixels and wavelength 532 nm.

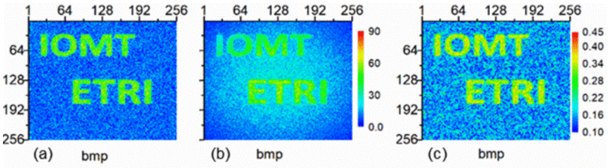

Figure 16 Ground truth activity maps for an object with two logos and uniform background: (a), non-normalized MSF estimate at uniform illumination and (b), - at Gaussian illumination, (c), normalized MSF estimate at Gaussian illumination, τ_{cl} =10Δ , τ_{cb} = 40Δ , N = 256, τ = 10 Δt.

The activity maps generated from the BMP images serve as the GT maps. These maps, shown in Figure 16, reflect uniform and Gaussian illumination conditions and are evaluated using the non-normalized and normalized MSF estimators

The objects were simulated with uniform and non-uniform illumination. Speckle images were compressed to 2-, 3-, and 6-times smaller size than the BMP images. SSIM maps were computed to compare the activity maps from the BMP and the decompressed JPEG and JPEG2000 images (Figure 17). Even at high compression levels, the higher activity regions corresponding to the logos are correctly identified. Reducing the image memory size by half using JPEG or JPEG2000 compression maintains a high similarity to the GT map for the activity maps from the decompressed images. Further reduction in image memory size introduces artifacts, particularly the blocking artifacts typical of JPEG compression. The JPEG2000 algorithm shows better preservation of similarity to the GT map, especially in the higher activity regions. While similarity to the GT map is important, the critical requirement is the ability to differentiate regions of different activity. The observed artifacts primarily affect the background and do not interfere with the accurate representation of activity in the test object. This indicates that lossy JPEG or JPEG2000 compression is suitable for visualizing spatial regions with varying process speeds.

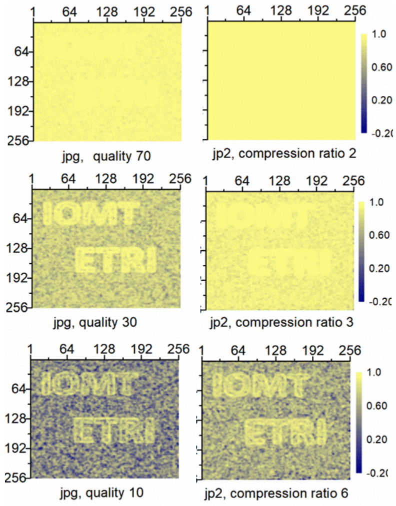

Figure 17 Maps of SSIM for comparison of activity maps from decompressed and bmp images for an object with two logos and uniform background under uniform illumination (non-normalized MSF estimate); type and degree of compression are given under each map, $\tau_{cl} = 10\Delta$, $\tau_{cb} = 40\Delta$, $N = 256$, $\tau = 10\ \Delta t$.

3.1.2 Compression of experimental speckle images

We demonstrated the applicability of JPEG and JPEG2000 compression for real dynamic speckle measurements by analysing data from two drying experiments.

The first experiment involved a metal coin coated with non-transparent paint. This object, with its intricate relief of grooves and embossments, provided an excellent test case to evaluate how compression affects the visualization of activity due to the varying evaporation speeds of paint across different surface features. Exemplary speckle images for the coin in BMP format, and their decompressed JPEG and JPEG2000 versions, are shown in Figure 18.

The second experiment focused on capturing speckle images of a droplet of water and methanol solutions containing the azopolymer PAZO at different temperatures.

Images were captured by a Baumer X06c-s CMOS camera with 780×582 pixels at an 8.1 μm pixel pitch. The images were recorded with a 20 μs exposure time and a 250 ms interval Δt between frames. The environment was maintained at 25°C, and the objects were illuminated by a He-Ne laser at 632.8 nm on a vibration-isolated table. We used a PAX5710VIS-T polarimeter to verify the linear polarization of the light.

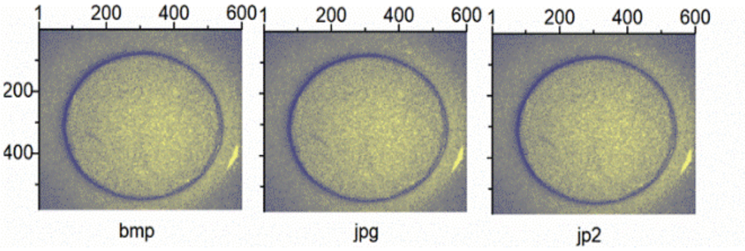

Figure 18 Image plots for speckle data recorded in bmp, jpg and jp2 formats in the drying experiments with a coin covered with paint

The GT maps and the activity maps from decompressed JPEG and JPEG2000 images in the coin experiment are shown in Figure 19 and Figure 20. Given the non-uniform illumination of the coin surface, the activity maps were extracted using a normalized estimate to compensate for the non-uniform intensity distribution, resulting in better accuracy. JPEG files were recorded at quality levels of 95, 90, 70, 50, and 30, resulting in compressed image memory sizes of 138 KB, 80.8 KB, 36.4 KB, 23.9 KB, and 15.0 KB, respectively. The resulting activity maps effectively reflected the coin's relief with good spatial resolution, particularly for compression quality settings of $Q \geq 50$. Compression at $Q = 50$ provided about 55 times reduction in memory size with acceptable map quality, although further size reduction led to a decline in quality. The JPEG2000 maps at the highest compression ratios (η = 50 and 60) also showed acceptable visualization quality, outperforming JPEG overall in activity visualization while still allowing high compression ratios.

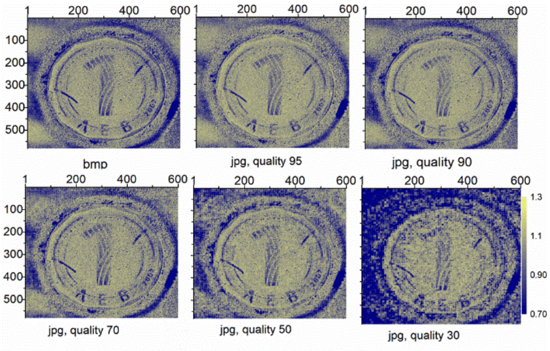

Figure 19 Activity maps for a coin covered with paint; maps are built from 256 decompressed jpg images recorded with different quality and compared to the GT map from images in the bmp format; τ = 10Δt

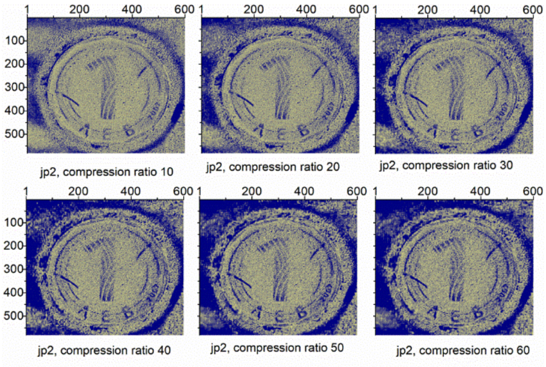

Figure 20 Activity maps for a coin covered with paint; maps are built from 256 decompressed jp2 images recorded at different compression ratios and compared to the GT map from images in the bmp format; τ = 10 Δt

For the droplet experiment, activity maps were computed for all image sets acquired at 30, 40, 50, and 60°C using the non-normalized and normalized estimators. Due to non-uniform intensity and lower reflectivity in the droplet, the normalized estimator was more suitable, but we presented the non-normalized estimator results to highlight compression-induced artifacts. Figure 21 compares GT maps from the 40°C set with maps from decompressed JPEG and JPEG2000 images compressed to 10, 20, and 30 times smaller sizes.

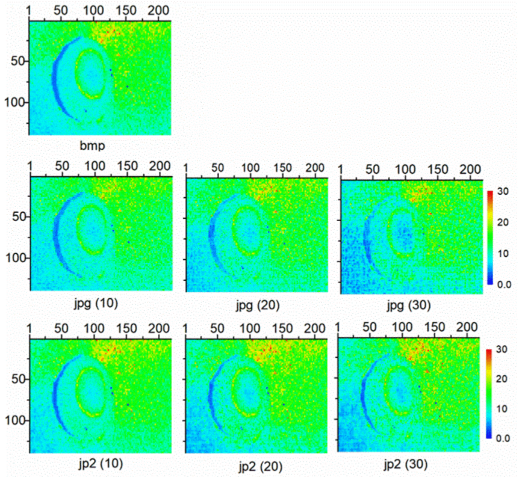

Figure 21 Comparison of non-normalized activity maps from decompressed images and from bmp images for a droplet of polymer solution; the numbers in the brackets show the ratio between the bmp and the compressed image sizes.

Despite visible artifacts, the maps remained informative. The mean SSIM for comparing the decompressed images to the GT maps was 0.924, 0.846, and 0.739 for JPEG, and 0.941, 0.892, and 0.791 for JPEG2000, across the different compression ratios.

In Figure 22, we plot the average MSF estimate over time for 60°C. The average MSF values for bmp and jpg images are quite similar, although the difference between the curves increases at $\eta = 10$ and decreases at $\eta = 20$. For the jp2 compressed images, the average MSF is higher than for the bmp images, and the difference between the bmp and jp2 curves grows with η and slightly with time. Despite this difference, jp2 compression provides a more accurate characterization of the polymer droplet drying process, as it is the relative changes in the estimate, rather than its absolute value, that are most informative.

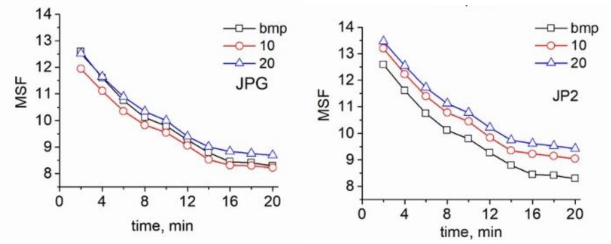

Figure 22 Drop of the non-normalized activity estimate in time for a drying droplet of a polymer solution at 60°C for processing of bmp and decompressed jpg (top) and jp2 (bottom) images at compression ratios 10 and 20.

To sum up, both JPEG and JPEG2000 formats provide high-quality activity visualization even at high compression ratios, such as a 50-times reduction in colour image size. However, as transform-based methods, JPEG and JPEG2000 change the temporal correlation of intensity values at each point depending on the compression ratio used.

3.2 Dynamic speckle imaging with SVD compression

Going further, we developed a method for compression of speckle images, which is based on SVD algorithm. Several decomposition approaches have been recently reported for processing of sequences of dynamic speckle patterns. In our approach, the DSI is implemented according to the following scheme: 1) recording of N correlated in time speckle images for a single activity map; 2) SVD compression of the images and storage of non-zero data; 3) calculation of activity map from decompressed images built from the non-zero data. The benefit from compression is the option to perform step 3 at any appropriate time after the acquisition.

The compression efficiency is assessed using both synthetic and experimental data. For comparison purposes, the experimental data sets are also compressed using the JPEG standard as a benchmark. The proposed algorithm effectively reduces storage size while preserving the quality of the activity map, comparable to the GT map generated from 8-bit encoded speckle images. The quality of the compressed data is evaluated using SSIM.

3.2.1 SVD compression of synthetic speckle images

As in our previous studies, first, we generated synthetic images. The synthetic speckle images generation is similar to the one described in Section 2.1.1.

3.2.1.1 Direct SVD compression of speckle images

SVD was applied to each image $I_n = \{I_{ik,n}; i = 1 \dots N_x, k = 1 \dots N_y\}$ in the sequence $I_1, I_2, \dots, I_N$. Each speckle image was decomposed into the product of three matrices, $I_n = U_n \Sigma_n V_n^T$, retaining only Q non-zero singular values in the diagonal matrices Σ_n for all $n = 1 \dots N$. This resulted in a sequence of decompressed images $J_n = U_n' \Sigma_n' V_n'^T$ for $n = 1 \dots N$, where U_n' and V_n' are composed of the first Q_{md} columns of U_n and the first Q_{md} rows of V_n, respectively, and the diagonal matrix Σ_n' is of size $Q_{md} \times Q_{md}$. The size of each recorded image in the sequence $I_1, I_2, \dots, I_N$ is $N_x \times N_y$. We then calculated the activity maps from the decompressed images $J_1, J_2, \dots, J_N$ corresponding to different numbers of modes Q_{md}, and determined the mean values and standard deviations of the

MSF estimate in the four activity regions of the test object with regions Z1, Z2, Z3 and Z4 described above. The results are shown in Figure 23. The last points on the plots, at Q_{md} = 512, represent the case of non-compressed bmp images. The size of this image is ….by…. pixels. Compression is achieved when Q_{md} is less than 256.

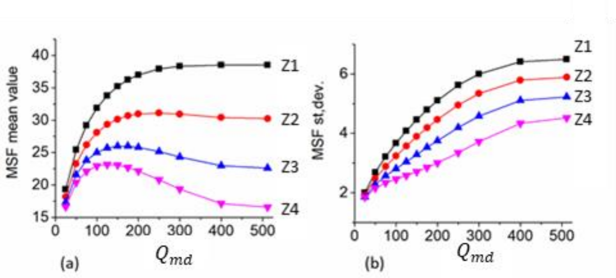

Figure 23 Mean values (a) and standard deviations (b) of the MSF estimate in the four activity regions of the synthetic object as a function of the number of non-zero modes, Q_{md}; time lag $\tau = 10\Delta t$, N = 256

The low contrast is a significant drawback, as illustrated in Figure 24, which presents maps obtained from the decompressed images $J_1, J_2, \dots, J_N$ at Q_{md} = 25, 50, 100, and 150. The maps at Q_{md} = 25 and 50 are of limited use for DSA and they also exhibit some artifacts. The maps at Q_{md} = 100 and 150 are more acceptable, especially with contrast enhancement techniques.

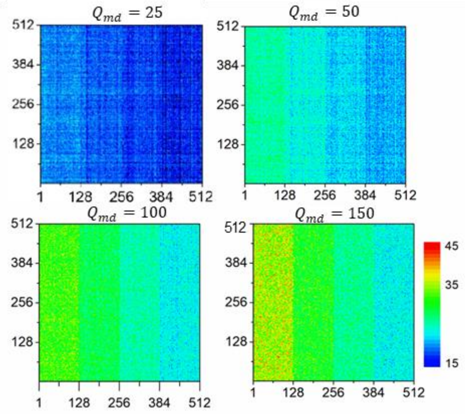

Figure 24 Activity maps for a synthetic object with four activity regions at different compression ratios: 10.24 (Q_{md} = 25), 5.12 (Q_{md} = 50), 2.56 (Q_{md} = 100), 1.7 (Q_{md} = 150), with a time lag $\tau = 10\Delta t$ and N + = 256.

This conclusion is further supported by the histograms of the MSF estimate at different Q_{md} values, shown in Figure 25. As Q_{md} decreases, the histograms become narrower, indicating reduced fluctuations in the estimate, but the overlap increases substantially. We observe that Q_{md} must be at least 100, suggesting that the benefit from SVD compression in this case of a grayscale image is rather modest, with a compression ratio of approximately 3:1.

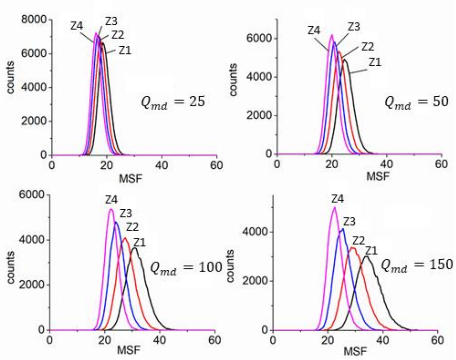

Figure 25 Histograms of the MSF estimate for a synthetic object with 4 activity regions at different compression ratios: 10.24 (Q_{md} = 25), 5.12 (Q_{md} = 50), 2.56 (Q_{md} = 100), 1.7 (Q_{md} = 150); time lag τ = $10\Delta t$

3.2.1.2 Image difference SVD compression

We proposed to compress the differences, $D_n = I_{n+1} - I_n$, $n = 1...N-1$. The arrays, D_n, $n = 1...N-1$ exhibit some structure due to the spatial distribution of the speed of the ongoing processes. The activity maps and histograms of the MSF estimate, that have been built at time lag $\tau = 10\Delta t$, $N = 256$ for a sequence $D_1{}'$, $D_2{}'$ . . . $D_{N-1}{}'$ restored after SVD compression of D_1, D_2 . . . D_{N-1}, are shown for Q_{md} = 10, 25, 50 in Figure 26

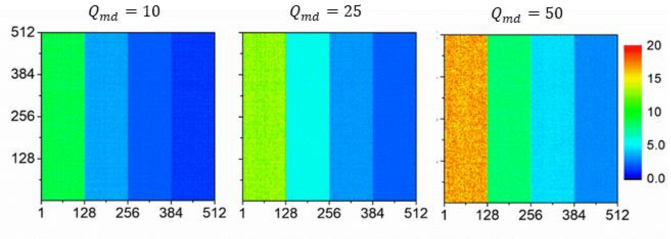

Figure 26 Activity maps for a synthetic object with 4 activity regions at different compression ratios: 25.06 (Q_{md} = 10), 10.24 (Q_{md} = 25), 5.12 (Q_{md} = 50); time lag $\tau = 10\Delta t$, N = 256.

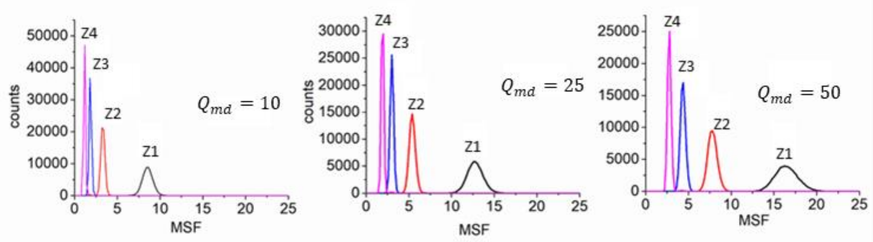

Figure 27 Histograms of the MSF estimate for a synthetic object with 4 activity regions at different compression ratios: 25.06 (Q_{md} = 10), 10.24 (Q_{md} = 25), 5.12 (Q_{md}= 50); time lag $\tau = 10\Delta t$, N = 256

The obtained maps show very good contrast. The histograms of the MSF estimate do not overlap. The decrease of Q_{md}leads to the decrease of the mean values of the estimate and the spread of the histograms. As it should be expected, the spread is the largest for the region Z1 with the fastest fluctuations of intensity. The activity areas can be easily distinguished even at Q_{md}= 10. In view that SVD compression inevitably leads to changes in spatial correlations between the intensity data in the decompressed images, the second SVD approach is more appropriate for objects with comparatively large activity regions.

3.2.2 SVD compression of experimental speckle images

For the experimental validation of SVD compression applied to speckle images in DSI, we selected two objects: 1) a coin coated with non-transparent paint, and 2) a droplet of water polymer solution spread on a glass substrate.

For the first object, the GT map and the activity maps generated from the image sequence $J_1, J_2, \dots, J_N$ with increasing numbers of modes Q_{md} at N = 256 and a time lag $\tau = 10\Delta t$, are shown in Figure 28 for the test object (the coin). All maps are plotted using the same scale. These maps were produced using a normalized MSF. The number of pixels used in the RGB colour images was 580×600, so the total number of recorded intensity values across the three channels was 3×580×600. This number was used to evaluate the compression ratio, considering that only $Q_{md}(1 + N_x + N_y) = 1181Q_{md}$ non-zero values were retained.

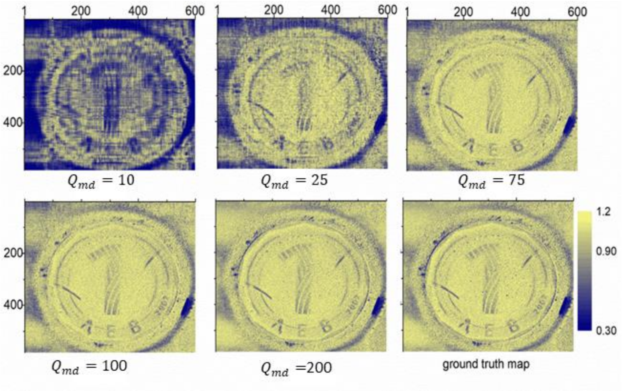

Figure 28 Activity maps for a coin covered with non-transparent paint at different compression ratios: 88.4 ($\mathrm{Q_{md}}$= 10), 41.8 ($\mathrm{Q_{md}}$= 25), 11.8 ($\mathrm{Q_{md}}$= 75), 8.8 ($\mathrm{Q_{md}}$= 100), and 4.4 ($\mathrm{Q_{md}}$= 200), with a time lag $\tau = 10\Delta\mathrm{t}$ and N = 256.

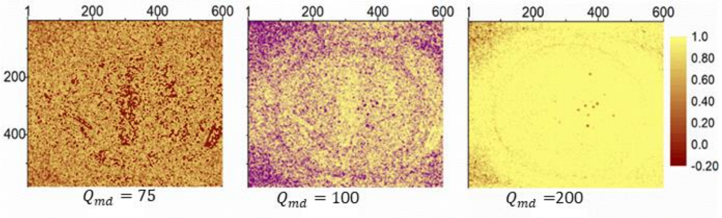

Figure 29 Structural similarity maps for the GT map of MSF estimate for a coin covered with non-transparent paint and activity maps at different compression ratios: 11.8 ($\mathrm{Q_{md}}$= 75), 8.8 ($\mathrm{Q_{md}}$=100), 4.4 ($\mathrm{Q_{md}}$= 200); time lag τ = $10\Delta t$, N = 256.

As shown in the figures, the activity maps increasingly resemble the coin's relief as the quality improves with increasing Q_{md}. The maps are deemed acceptable when $Q_{md} \geq 75$. The structural similarity index maps in Figure 29 suggest that results are acceptable when $Q_{md} \geq 100$.

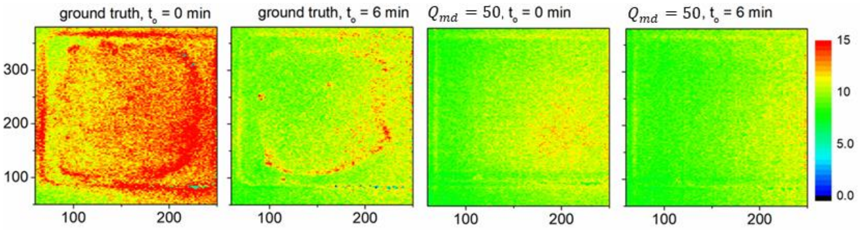

Figure 30 Ground truth map and activity map at Q_{md}= 50 for a droplet of polymer solution at the beginning of the experiment and at 6 minutes after; the maps are calculated by processing arrays of differences of successive images at time lag τ = $10\Delta t$, N = 256.

Figure 30 presents the activity maps obtained from the sequence $D_1{}'$, $D_2{}'$ . . .$D_{N-1}{}'$ composed at Q_{md}= 50 from the speckle images acquired for the second object. The time lag was τ = $10\Delta t$ and N = 256. The maps correspond to the MSF estimate (2.5). As it should be expected, the mean values of the estimate for the maps from the decompressed images are lower than for the ground truth maps. The maps at Q_{md}= 50 are smoother than the GT maps. In both cases, decrease of activity due to the drying is visible. Compression for Q_{md}= 50 is about 20 times.

3.3 Dynamic speckle imaging with PCA compression

We introduce a lossy compression method for speckle images using principal component analysis (PCA). The compression efficiency is assessed using both synthetic and experimental data. For comparison purposes, the experimental data sets are also compressed using the JPEG standard as a benchmark. The proposed algorithm effectively reduces storage size while preserving the quality of the activity map, comparable to the GT map generated from 8-bit encoded speckle images. The quality of the compressed data is objectively evaluated using SSIM. The reason why JPEG algorithm was chosen as a benchmark is because JPEG and PCA-based ones have a lot of similarities in their structure.

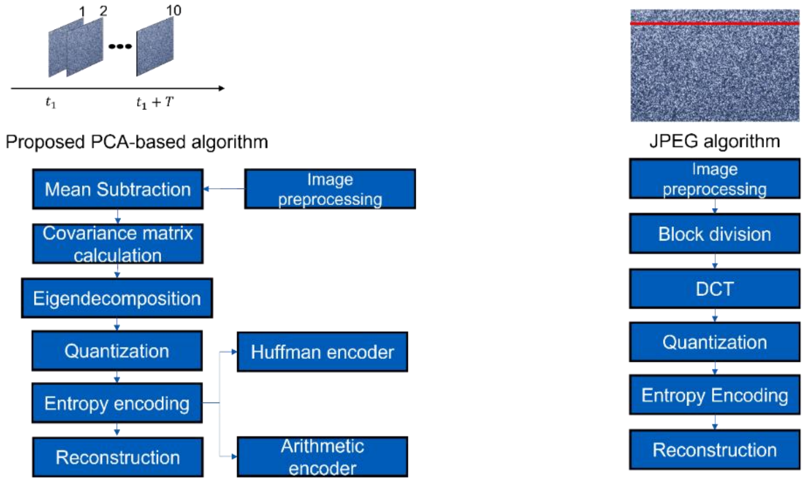

Figure 31 Structure of PCA-based compression algorithm and of JPEG algorithm

The algorithm consists of seven steps:

Step 1. Image Pre-processing: Pixels at a specific position (i, k) are extracted from all speckle images and assembled as an 1D vector. These 1D vectors are stored in a single array of size $v \times N$, where $v = N_x \times N_y$. This array is referred to as the data.

Step 2. Mean Subtraction: This step centres the data by subtracting the mean value, which enhances the efficiency of the compression algorithm by ensuring unbiased and accurate results.

Step 3. Covariance Matrix Computation: The temporal correlation within the speckle image sequence is estimated by calculating the covariance matrix.

Step 4. Eigen decomposition: The covariance matrix is decomposed into eigenvectors and eigenvalues. The data are then transformed by multiplying the data array by the eigenvectors, following the equation:

$$\text{PCA matrix} = (\text{data}(v \times N) - \text{mean value}) * E$$

where E is the eigenvector matrix of size $N \times N$

Step 5. Quantization: The transform coefficients are quantized. The quantization matrix determines the compression ratio and influences the degree of image quality loss.

Step 6. Entropy Encoding: The quantized coefficients are encoded using Huffman and arithmetic encoders. This reduces data redundancy by assigning shorter codes to more frequent symbols, resulting in efficient compression.

Step 7. Reconstruction: The compressed data are reconstructed by multiplying them with the transpose of the eigenvector matrix and adding the mean value back. The 1D vectors are then rescaled to recreate the 2D speckle images.

We developed two versions of the PCA-based compression algorithm: one using a Huffman encoder (PCA-CH) and the other with an Arithmetic encoder (PCA-CA). These algorithms were tested on simulated and experimental data.

3.3.1 Compression of simulated data

In the simulation, 100 speckle patterns of size 512×512 pixels were generated. As in previous simulations, we created speckle patterns with 4 different activity regions under uniform illumination. The GT map and activity maps based on the compressed speckle images at a quantization step $Q_{st} = 20$ and Q = 70 are shown in Figure 32. The compression ratio (C.r.), representing the number of uncoded to coded bits, and the SSIM values for the PCA-CH and PCA-CA algorithms are significantly higher compared to the SSIM of the activity map derived from JPEG-compressed speckle images.

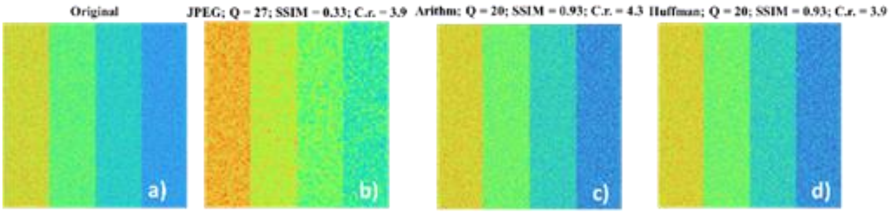

Figure 32 Activity maps of simulated images. Quantization step = 20. Quality = 70. a) original image; b) compressed with JPEG; c) compressed with PCA-CA; d) compressed with PCA-CH

For the second simulation we created 100 speckle patterns of size 512×512 which simulate circular regions of different activity. In addition, we simulated non-uniform illumination of the circular sample. Below are shown the results for the case when Q_{st} = 20 and JPEG Q = 50. It is clearly visible that the PCA algorithm compresses data much more efficiently comparing to JPEG. While c.r. is the same for all images, SSIM significantly differs: 0.68 vs 0.85 for JPEG and the PCA methods respectively.

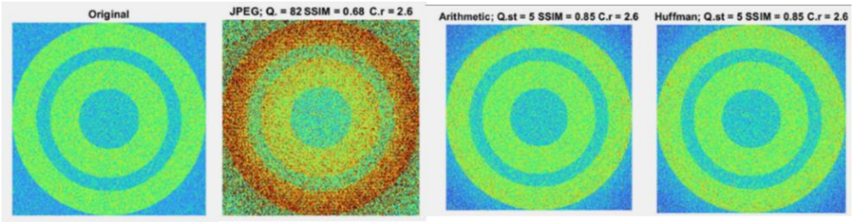

Figure 33 Activity maps of simulated images for the case of non-uniform illumination. Quantization step = 20, Q = 50; a) original image; b) compressed with JPEG; c) compressed with PCA-CA; d) compressed with PCA-CH

3.3.2 Compression of the experimental data

For experimental data, we used 100 images capturing the drying process of an azopolymer PAZO solution on a glass. We analysed two data sets with different resolution: 1280×900 and 280×200. Images were compressed at three quantization steps (Q_{st} = 5, 20, 40) for both PCA-CA and PCA-CH, and three Q values (96, 87, 70 for the higher resolution and 92, 69, 37 for the lower one) for JPEG compression. The highest compression ratio was achieved for PCA-CA, with PCA-CH showing slightly lower performance, especially at Q_{st} = 40. The JPEG quality values were selected to match the compression ratio of PCA-CA. An example of an original speckle image with PAZO solution and its compressed versions at Q_{st} = 5 and Q = 90 are shown in Figure 34. The SSIM value for JPEG is 0.96, while PCA achieves 0.99 with a higher compression ratio, indicating that the PCA algorithm yields more efficient results.

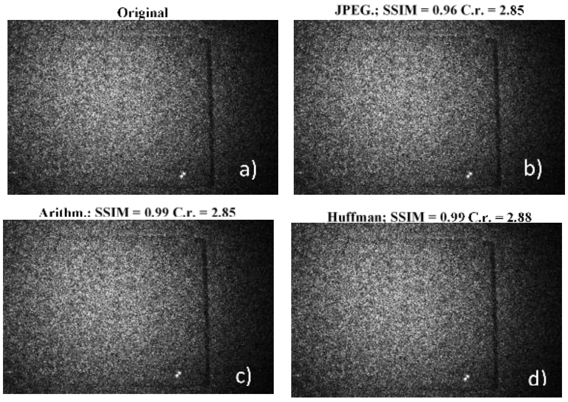

Figure 34 First speckle image of the test set with resolution 280×200. Quantization step = 5, Q = 90; a) original image; b) compressed with JPEG; c) compressed with PCA-CA; d) compressed with PCA-CH

It's important to note that SSIM values for activity maps are generally lower than those for speckle images. For instance, for speckle set of resolution 280×200 at Q_{st} = 5 and Q = 90, the SSIM for speckle images is 0.96, while it is 0.97 for activity maps (Figure 35.1). This difference is due to the impact of compression algorithms on the time correlation of images, which is crucial for the DSI methods.

As image number increases, correlation coefficient value reduces. As the quantization step increases, so does the compression ratio. At Q_{st} = 20, the difference between JPEG and PCA-based activity maps is most evident, with SSIM values of 0.78 for PCA-CA and 0.59 for JPEG. Moreover, JPEG compression results in unsatisfactory outcomes (Figure 35.2c), as the activity map contains block artifacts. However, artifacts are only visible on low resolution. For images with 1280x900 pixels, there are no block artifacts (Figure 36). In the final experiment at Q_{st} = 40 and Q = 37, the polymer drying process in the right glass corner is barely visible, with the SSIM of PCA activity maps at 0.58. Further increasing the quantization step is not advisable, as the high compression ratio diminishes the correlation between images.

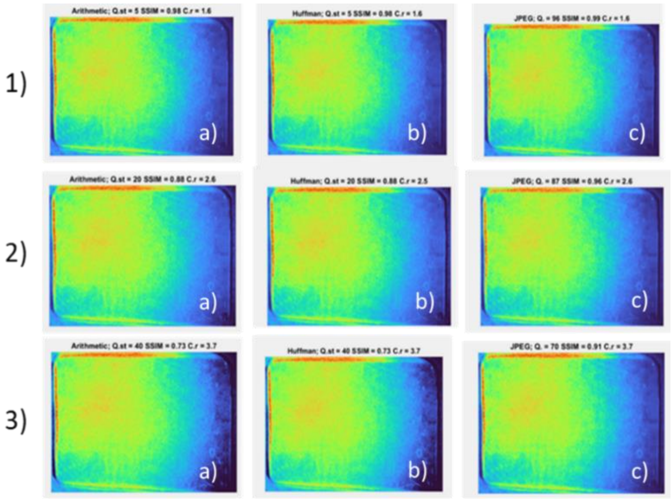

Figure 35 Calculated activity maps for PAZO solution (1280×900) based on compressed speckle images; a) compressed with PCA-CA; b) compressed with PCA-CH; c) compressed with JPEG; 1. Quantization step = 5. Quality = 96; 2. Quantization step = 20. Q = 87. 3. Quantization step = 40. Quality = 70

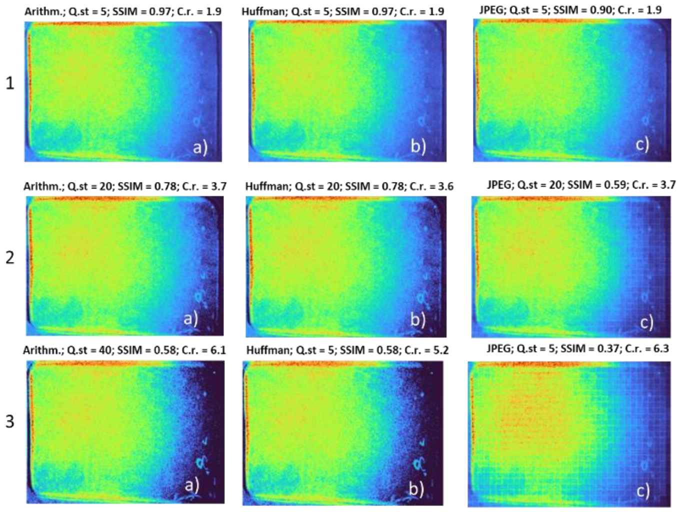

Figure 36 Calculated activity maps for PAZO solution (280×200) based on compressed speckle images; a) compressed with PCA-CA; b) compressed with PCA-CH; c) compressed with JPEG; 1. Quantization step = 5. Q = 92; 2. Quantization step = 20. Q = 69. 3. Quantization step = 40. Q = 37

3.3.3 Compression of speckle images with non-uniform illumination

In the next experiment we compressed speckle images of circular object under non-uniform illumination. The surface of the circular sample was covered with the TAMIYA X2 paint. We built activity maps based on images with size 500x500. Same as in previous experiments, Q_{st} for PCA algorithms are 5, 20 and 40. JPEG Q levels are relatively 87, 70 and 60.

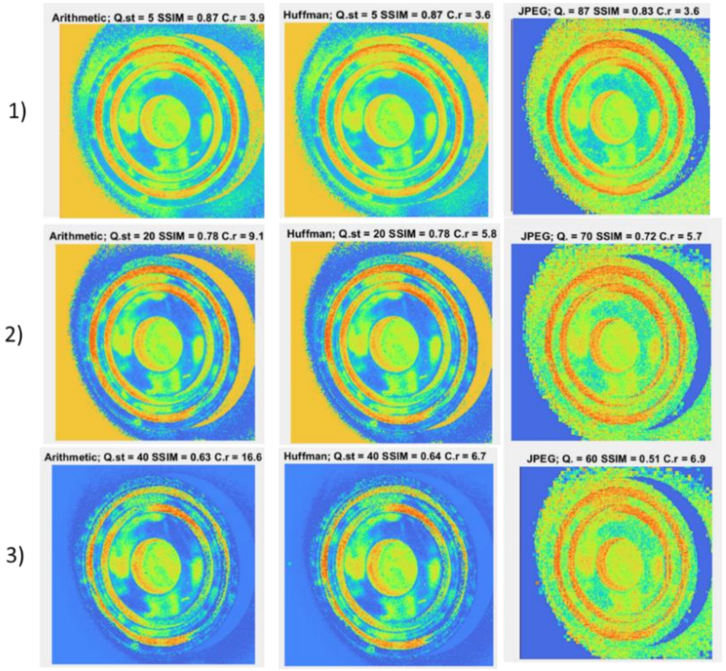

Figure 37 Calculated activity maps for the circular object covered with TAMIYA X2 paint based on compressed speckle images; a) compressed with PCA-CA; b) compressed with PCA-CH; c) compressed with JPEG; 1. Quantization step = 5. Q = 87; 2. Quantization step = 20. Q = 70; 3. Quantization step = 40. Q = 60

At Q_{st}= 5 and Q = 87, the SSIM for speckle images compressed with PCA is 0.97 while it is 0.83 for JPEG images (Figure 37). At Q_{st}= 20, the difference between JPEG and PCA-based activity maps is most evident, with SSIM values of 0.78 for PCA-CA and 0.72 for JPEG. Like in previous experiments, JPEG compression results in block artifacts. In the final experiment at Q_{st} = 40 and Q = 60, the paint drying process is still visible. SSIM of PCA activity maps is 0.63 and 0.64 vs 0.51 for JPEG. Moreover, PCA-CA algorithms show its higher efficiency as its c.r. is 16.6 vs 6.7 for PCA-CH while maintaining the same quality.

Chapter 4 Application of dynamic speckle imaging in non-destructive testing

The studies in the Fourth Chapter refer to author's papers A8 – A10.

4.1 Portable low-cost set-up for outdoor implementation of dynamic speckle analysis

Most laboratory DSA experiments are typically performed in controlled environments using specialized equipment, such as vibration-isolated tables, high-end cameras, high-quality lasers, and beam expanders. This equipment is impractical for field conditions and is often prohibitively expensive for many companies. We propose a miniature portable device, based on a low-cost laser attached to a smartphone, and checked its efficiency under the field conditions. A strong argument for using a portable set-up is the fact that the absolute values of the speckle intensity are not needed to construct a reliable activity map.

In contrast to the stationary laboratory setup shown in Figure 38, where the laser dimensions are not critical, designing a portable laser for DSA requires careful consideration of the size and weight of the housing, which are crucial parameters.

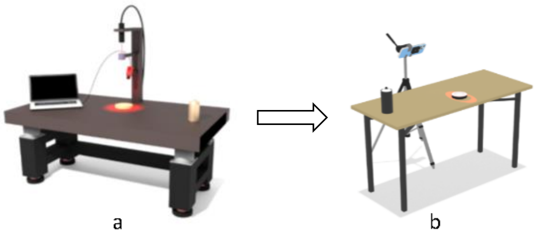

Figure 38 Stationary laboratory dynamic speckle setup (a); proposed portable DSA setup (b)

4.1.1 *Simulation*

Simulation of the speckle patterns was done as described in Section 2.3.1. Noise sources such as the shot noise from the ambient light and quantization noise from 8-bit image encoding were considered. To simulate correlation radius variation, we composed a synthetic object to correspond to the object comprising two regions as 3 mm deep cut-outs. The regions contain more paint in a drying experiment, thus slowing the evaporation process. Under uniform illumination, the non-normalized MSF was applied to estimate activity. This estimate demonstrates good sensitivity, crucial for processing data in noisy environments. Figure 39 shows simulation results for three cases of activity distribution: i) case A with temporal correlation radii of 10 Δt and 40 Δt, ii) case B with radii of 15 Δt and 40 Δt, and iii) case C with radii of 20 Δt and 40 Δt. The time lag corresponded to the smaller temporal correlation radius. At a wavelength of 635 nm, 200 images were processed with size of 256×256 pixels. The background region had a temporal correlation radius of 100 Δt. High values of the noise parameters were chosen to simulate the impact of both vibration and shot noise from ambient light. As observed, both types of noise increase intensity fluctuations in all regions, with vibration phase noise having a more pronounced effect.

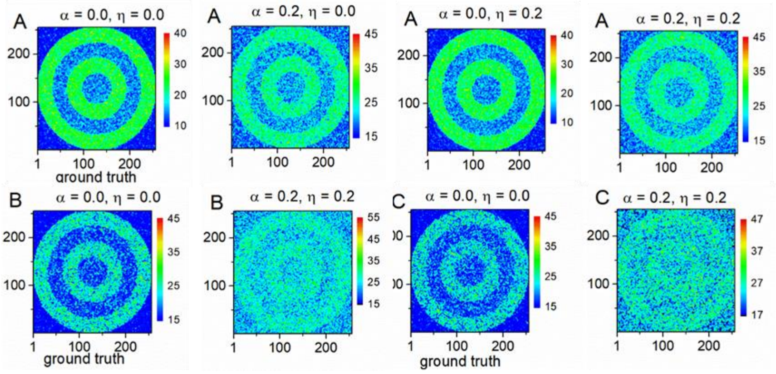

Figure 39 Activity maps as 2D distributions of non-normalized MSF estimate (2.5) in the presence of the environmental noise for uniform illumination at wavelength 635 nm and $N = 200$, image size 256×256 pixels; A: the temporal correlation radii are 10 Δt and 40 Δt, B: the radii are 15 Δt and 40 Δt, C: the radii are 20 Δt and 40 Δt; the time lag is equal to the smaller temporal correlation radius.

4.1.2 Experimental results

For experimental validation, we captured speckle images of a cylindrical object with circular cut-outs that was coated with Tamiya Mini X-2 white paint. Subsequent experiments were conducted using a portable laser and a smartphone camera. Speckle images were captured using a Xiaomi Mi 9T smartphone, which was connected to a PC either as an IP camera or a USB camera. In the final set of experiments, the speckle images were stored directly in the smartphone's memory and then transferred to the PC after recording.

For each experiment, 10 activity maps were generated from 200 speckle images acquired at 300 ms intervals, resulting in one activity map per minute of the paint drying process. To compare the results, three activity maps corresponding to the first, fifth, and tenth minutes of the experiment were selected. Figure 40 shows the activity maps based on GT speckle images, where high contrast is clearly visible.

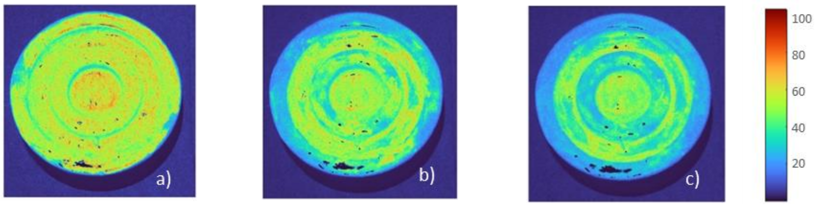

Figure 40 Activity maps based on original speckle images: (a) 1st minute; (b) 5th minute; (c) 10th minute

Using the iVCam software reduces the quality of speckle images, thereby affecting the final quality of the activity maps (Figure 41). This quality reduction occurs because the captured images are compressed using the JPEG standard at a high compression level. Image degradation and artifacts caused by JPEG compression are noticeable on the activity maps with a resolution of 1920×1080. Despite this visual drawback, JPEG compression does not critically affect the time correlation of speckle images, and even low-quality activity maps clearly show the activity changes during the experiment.

In the next experiment, data were transferred to the PC via a USB cable (Figure 42). At 1920×1080 resolution, similar image quality degradation and artifacts are observed. Connecting the smartphone to the PC via USB allowed for faster image transfer compared to Wi-Fi.

In both USB and Wi-Fi connections, the drying process can be clearly tracked. However, the absolute values of the MSF estimate are lower compared to activity maps based on speckle images captured under laboratory conditions.

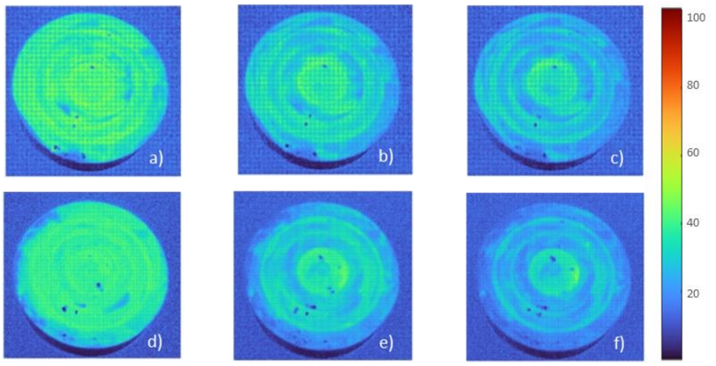

Figure 41 Activity maps based on speckle images captured with the Xiaomi Mi9T camera connected to the PC via Wi-Fi with resolution: 1920×1080 (a) (b) (c) and 3840×2160 (d) (e) (f); 1st minute – (a) (d); 5th minute – (b) (e); 10th minute – (c) (f)

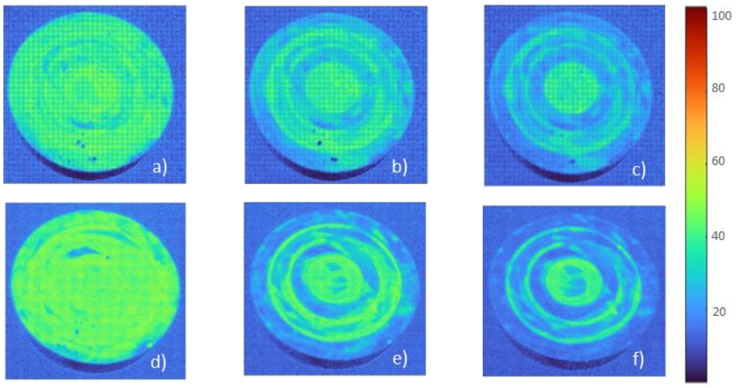

Figure 42 Activity maps based on speckle images captured with the Xiaomi Mi9T camera connected to the PC via USB with resolution: 1920×1080 (a) (b) (c) and 3840×2160 (d) (e) (f); 1st minute – (a) (d); 5th minute – (b) (e); 10th minute – (c) (f)

In the final experiment, the speckle images were captured and stored on the smartphone, then transferred to the PC for processing after the experiment was completed. Some activity maps for the first, fifth, and tenth minute are shown in Figure 43. The contrast of the maps obtained in this experiment is higher compared to the previous ones.

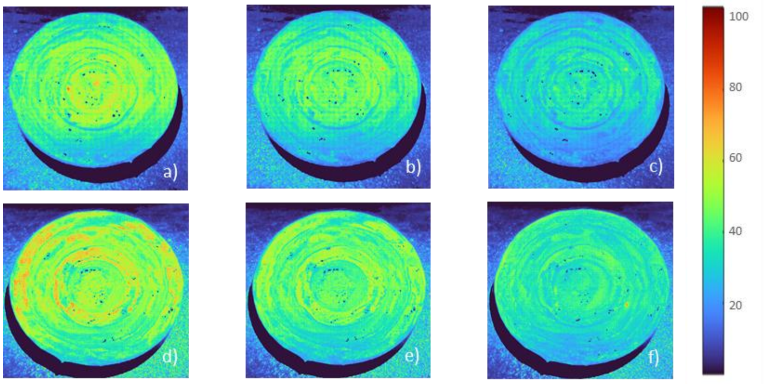

Figure 43 Activity maps based on speckle images captured with Xiaomi Mi9T with resolution: 1920×1080 (a) (b) (c) and 3840×2160 (d) (e) (f). Images are stored in the smartphone’s memory; 1st minute – (a) (d); 5th minute – (b) (e); 10th minute – (c) (f)

4.2 Implementation of dynamic speckle imaging with a high-speed camera for impact testing of composites

As a continuation of our study, we checked the DSI potential for damage and impact characterization. The experiment included impact testing with a gas gun of metal and composite plates by using a stereoscopic Digital Image Correlation (DIC) with two high-speed cameras. In addition to the DIC measurement, the DSI was implemented with laser illumination and high-speed camera acquisition. The main purpose of the DSI experiment was to characterize the impact by processing dynamic speckle data captured under extreme conditions. The DIC experimental setup consisted of white light sources, two high-speed cameras, FASTCAM Mini AX200 and FASTCAM NOVA S6 for image capturing and a gas gun with an impact speed of 55 m/s. For DSI experiments Photron FASTCAM Mini AX200 camera, Coherent Verdi 6 W (532 nm) laser and a gas gun were used.

4.2.1 Processing of printed speckle patterns with DIC

Application of the DIC method with VIC-3D software to the Cytec 977-2 CFRP plate gives estimation of displacement Z in mm and strain during deformation.

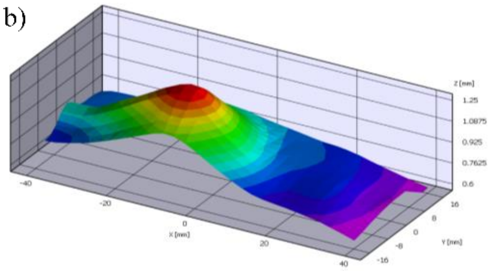

Figure 44 Moment of Cytec 977-2 CFRP sample deformation detected with the DIC method

4.2.2 Processing of laser speckle patterns

In the case of the DSI experiment, the raw data consist of large number of images characterized by low temporal correlation as the observed process leads not only to rapid pointwise fluctuations of intensity but also to fast changes of speckle intensity distribution in space and time.

To estimate activity for the extremely fast-developing impact process, first, we found the absolute value of the difference of intensities in two compared images, $D_{ik,n}^{m} = \left|I_{ik,n} - I_{ik,n+m}\right|$. The array of the differences is partitioned into rectangular blocks of $L\times M$ pixels where the condition $L>>M$ is fulfilled. The array was partitioned twice: i) with the L side parallel to the vertical Y axis and ii) with the L side parallel to the horizontal X axis [27].

Next, the mean values of the difference in all rectangular blocks were found for both orientations. Thus, there were enough pixels in the averaging area to decrease the fluctuations of the estimate of the mean and to provide high spatial resolution along one of the spatial axes. We built the following estimate of activity:

$$A_{ik,n}^{m} = V_{i'k',n}^{m} + H_{i''k'',n}^{m},\ i' = floor(i/L), k' = floor(k/M); i'' = floor(i/M),$$
$$k'' = floor(k/L) \qquad 4.1$$

where the estimates $V_{i'k',n}^{m}$and $H_{i''k'',n}^{m}$are the mean values

$$V_{i'k',n}^{m} = \frac{1}{LM}\sum_{c=i'L+1}^{(i'+1)L}\sum_{v=k'M+1}^{(k'+1)M} D_{cv,n}^{m}.\ H_{i''k'',n}^{m} = \frac{1}{LM}\sum_{c=i''M+1}^{(i''+1)M}\sum_{v=k''L+1}^{(k''+1)L} D_{cv,n}^{m} \qquad 4.2$$

We made experiments with three types of samples of size 200×200 mm for impact testing: 1) Aluminium plate 3 mm thick; 2) Woven thermoplastic CFRP 3 mm thick; 3) Cytec 977-2 CFRP 4 mm thick.

Here we described the experiment with woven thermoplastic CFRP 3 mm thick plate. The camera recorded the images of speckle patterns with resolution 256×128px before and after the impact. Figure 45 shows the images of speckle patterns acquired four consecutive moments after the shot of the gas gun. As is seen, there are strong variations in the spatial distribution of speckle intensity during the experiment.

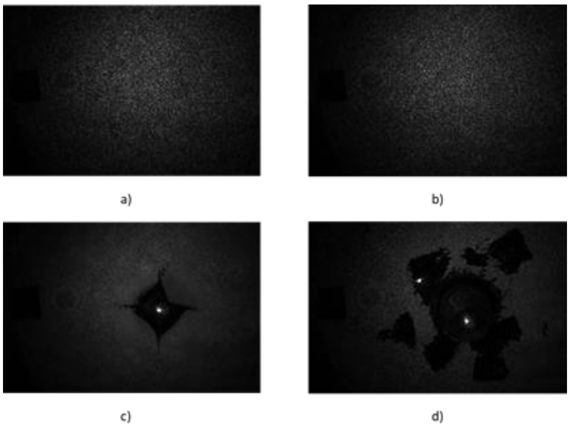

Figure 45 Woven thermoplastic CFRP 3 mm thick plate deformation a) image 51000 b) image 51200 c) image 51300 d) image 51400

To visualize the change in speckle statistics, we plotted the intensity sequences in the pixels (32,64), (32,192), (64,128), (96,64), (96,192) (Figure 46); the first number gives the row and the second – the column in the image.

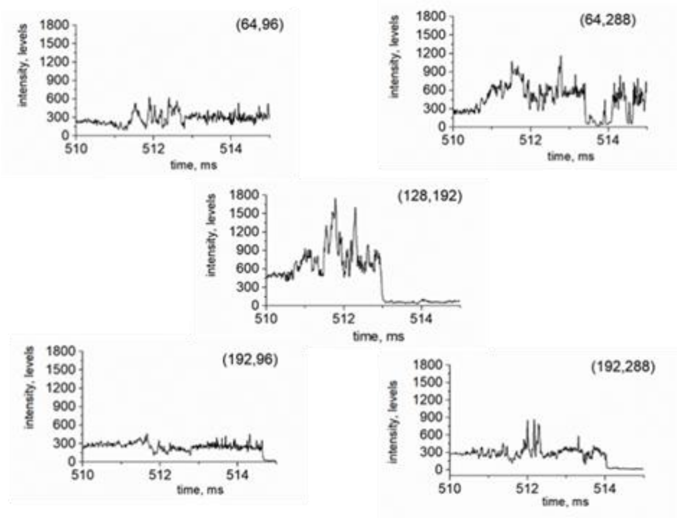

Figure 46 Time variation of speckle intensity for the woven thermoplastic CFRP 3 mm thick plate deformation at 5 different pixels.

The results clearly indicate that speckle statistics strongly varies in time and is rather different before and after the impact.

Activity maps at time lag 2 showing deformation of woven thermoplastic CFRP 3 mm thick plate are shown in Figure 47 in the range 510 ms to 514 ms after the shot was made. The chosen time lag is equivalent to time interval of 20 µs between the compared images.

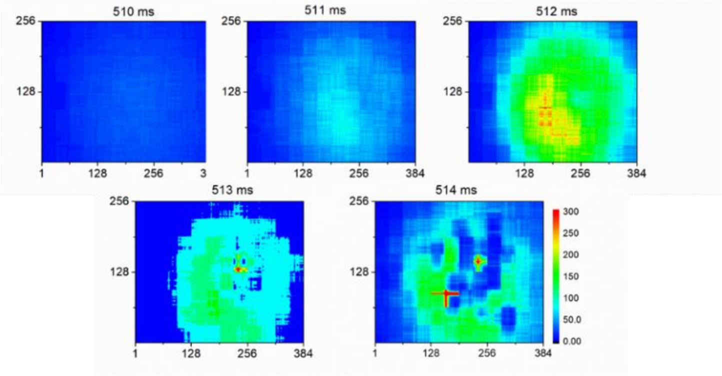
510 ms 511 ms 512 ms 513 ms 514 ms

Figure 47 Activity maps showing deformation process of woven thermoplastic CFRP 3 mm thick plate

To check whether there is temporal correlation in the sequence of the acquired images, we built activity maps corresponding to the time instant 512 ms at different time lags 1,2,3 and 4 (Figure 48). In case of correlation, the higher the time lag, the higher is the estimate value. As it can be seen, although the process is very fast developing, temporal correlation within tens of microseconds between the speckle images is evident.

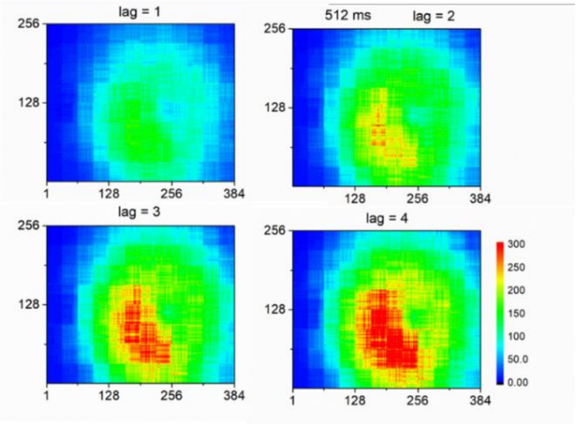
lag = 1 512 ms lag = 2 lag = 3 lag = 4

Figure 48 Activity maps at instant 512 ms at different time lags 1,2,3,4

We characterized the impact by introducing a threshold for activity estimate equal to 80. Figure 49 depicts change in time of the spatial area with activity above the threshold in the range from 511.2 ms to 512.8 ms. We see that the DSA provides valuable information about the spread of the higher activity area before and after the impact.

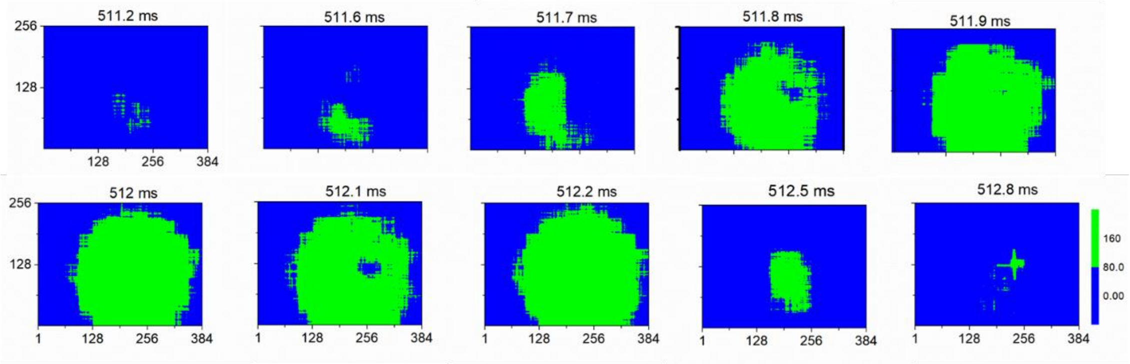
511.2 ms 511.6 ms 511.7 ms 511.8 ms 511.9 ms 512 ms 512.1 ms 512.2 ms 512.5 ms 512.8 ms

Figure 49 Activity maps with threshold 80 at instances in range 511.2 ms to 512.8 ms

4.3 Application of DSI in the non-destructive testing field

We studied ability of the DSA to detect a hidden defect in a sample subjected to tension at a certain tensile speed. The tensile loading is needed to excite dynamic speckle. The DSA method in this case is known as laser speckle photometry (LSP).

4.3.1 Tensile loading set-up for laser speckle photometry

Speckle excitation is achieved by sample stretching using a test machine (AMETEK LRX PLUS). A He-Ne laser (LASOS Lasertechnik) emitting at 632.8 nm is used. Light polarization is adjusted with a half-wave plate (fast axis at - π/4 to the loading axis). After the 4f spatial filter, the light beam is expanded and illuminates normally the sample. A camera (BASLER acA4096-30um) with its optical axis at 9.6 degrees with respect to the laser beam axis, acquisition rate 1/Δt equal to 30 frames per second and exposure time 0.01 s acquires a sequence of images of speckle patterns formed on the sample. The acquisition time *T* was usually 30 s. The photo of the set-up is given in Figure 50.

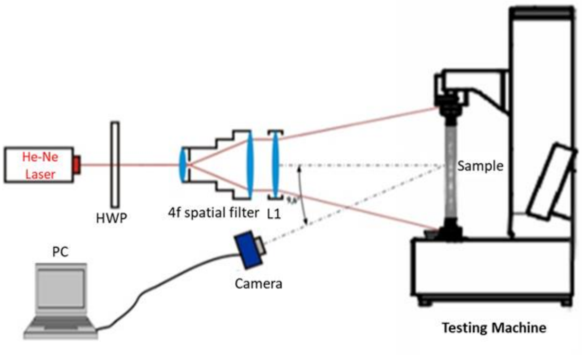

Figure 50 LSP set-up with speckle excitation under tensile loading

A test experiment with a rubber sample and a hole as a stress concentrator was performed. The sample was subjected to tensile stress at different tensile speeds: 1 mm/min, 5 mm/min, 10 mm/min, and 20 mm/min. To build activity maps, normalized MSF was used. We build 3 sets of activity maps presented in Figure 51 at different time lags: 1 Δt (top row), 5 Δt (middle row) and 10 Δt (bottom row). The maps corresponding to the four tensile speeds are denoted as A, B, C and D. Speckle excitation is observed for all tensile speeds. Rise of activity is clearly seen with the time lag and the tensile speed. In regions around the hole, activity is higher compared to regions where the sample does not contain stress concentrators. Thus, we established that LSP shows high sensitivity even at small tensile speeds as 1 mm/min when the extension of the upper border of the sample between two consecutive frames is less than a micrometre.

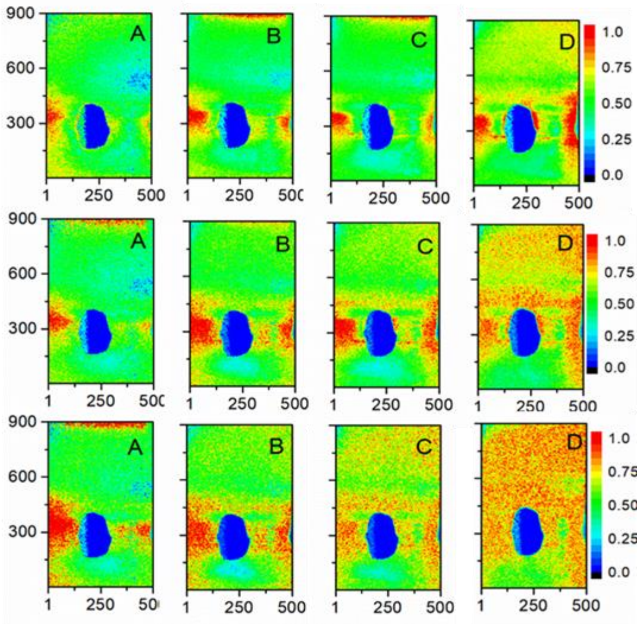

Figure 51 Normalized activity maps for a rubber sample with a circular hole at a tensile speed 1 mm/min (A), 5 mm/min (B), 10 mm/min (C) and 20 mm/min (D); top - time lag 1Δt, middle – time lag 5Δt, bottom – time lag 10Δt.

4.3.2 Hidden defect detection

After we have proven high sensitivity of the LSP with speckle excitation by stretch the sample, we proceeded with hidden defect detection. A rubber sample from a Land Rover Sport fender liner part with thickness of 5 mm was used. The length of the sample was 200 mm and the width – 50 mm. The defect represented a depression created by melting the rubber using a soldering iron at a temperature of 340°C. The defect was located within the borders of a rectangle of size 30 mm along the vertical (extension) direction and 10 mm in horizontal direction. The depth of the depression varied from 0.5 mm to 2 mm. The stretching of the sample continued for 30 seconds and was performed at different constant extension speeds starting from 1 mm/min and going up to 20 mm/min. The maps shown in Figure 52 and Figure 53 were obtained by averaging over 128 and 256 images or for the time intervals 4 s and 8 s respectively and tensile speed of 10 mm/min. The used small time lags of 0.033 s and 0.1 s guaranteed lack of decorrelation.

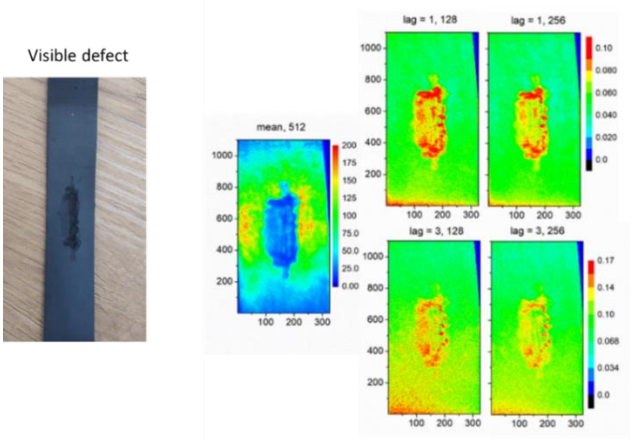

Figure 52 Normalized activity maps for a rubber sample with a visible defect at a tensile speed 10 mm/min; top - time lag 1 Δt, bottom – time lag 3 Δt.

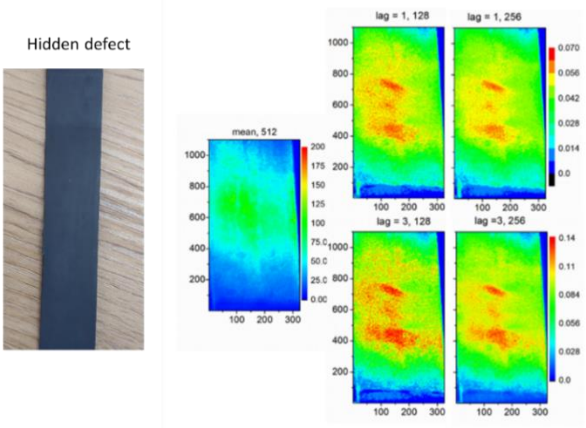

Figure 53 Normalized activity maps for a rubber sample with a hidden defect at a tensile speed 10 mm/min; top - time lag 1 Δt, bottom – time lag 3 Δt.

We built the mean intensity distributions for the speckle patterns captured for both sides of the sample. Much lower intensity in the region of depression was obtained compared to the surrounding area. Nevertheless, by using the normalized estimate we obtained that activity in this region is higher than on the remaining rubber surface. The maps obtained for the other rubber side definitely show an area of higher activity corresponding to the defect location within the sample. The mean intensity distribution in this case shows monotonous decrease of intensity to the periphery of the sample. The same experiment was repeated for a rubber sample with three smaller in size defects created in the same manner. The activity maps calculated from the images taken for the side of the sample where the defects are not visible also exhibit three spots of higher activity.

Conclusion

By capturing and analysing speckle patterns formed on the sample's surface when illuminated with the coherent light, DSI allows the detection of microscopic motion and structural changes. Although the development of DSI began in the 60s, when the first lasers appeared, there are still many tasks in this area to improve the technology.

In the Chapter 2, studies of various aspects of dynamic speckle analysis were presented. First, we have studied normalization in intensity-based DSA for processing raw speckle data with spatially varying statistics, as e.g. under non-uniform illumination. We proposed and studied modifications of algorithms which use for normalization at a given instant a sum of two intensities or a single intensity. We checked efficiency of the algorithms by applying them to low and high contrast simulated data and also compared them with processing of binary patterns as another approach for dealing with varying speckle statistics in the acquired images. We have proven that the pointwise algorithms in which normalization is done at each instant by using one or two intensity values are more efficient than the algorithms applying the time-averaged estimates of the mean value and the variance of speckle intensity.

We have analysed options for temporal resolution improvement in the pointwise dynamic speckle imaging. We have carried out set of simulations and an experiment in order to study influence of acquisition time T, which gives the temporal resolution, on quality of activity maps. We found out that $\Delta t \approx \tau_c$ worsens the MSF map contrast. Best quality was obtained in the case when Δt is a few times less than τ_c. When Δt is 100 times less than τ_c, the PDFs are narrower, but they ovelap significantly, which leads to map contrast decreasing. Nevertheless, visualization of regions of different activity is possible which directly means that improvement of the temporal resolution by choosing $\Delta t \ll \tau_c$ is feasible.

We developed a modified intensity-based algorithm for tracking dynamics of fast-developing processes in objects by using a sequence of correlated in time speckle patterns on their surface as input data. A given activity map is calculated by partitioning two images into overlapping segments with a small number of pixels. The estimate at a given point of the map is obtained by averaging within a segment. The dynamics can be characterized by processing at more than one time lag. The smaller the time lag, the better the temporal resolution of the algorithm. A small time lag, however, may lead to a low contrast map and poor visualization of activity due to the strongly fluctuating in space values of the estimate. Usage of a small segment size intensifies these fluctuations. For the experiment, the algorithm made possible visualization of the drying process of a drop of a polymer dissolved in a methanol. The obtained set of activity maps allows for tracking the drying process with good temporal resolution.

We have proved that the outdoor acquisition provides reliable data for an intensity-based pointwise DSA. Despite the strong fluctuations of the map data, it visualizes the spatial distribution of the degree of temporal correlation in the input data. An analysis of the DSA stability to noise sources is an integral part of this realization and answers the question of the DSA efficiency under outdoor conditions. Obviously, it is applicable to a certain level of noise, and it is crucial to determine this level. A noise analysis made in the thesis studied the impact of (1) the environmental phase noise due to the lack of vibration isolation and (2) the increased shot noise due to ambient light. From the noise sources affecting the activity map, we included in the analysis the shot noise from the laser photons and quantization noise. The validation of the outdoor measurement took into account the two requirements of the DSA implementation. The first is the mainly qualitative character of the DSA output. The activity map simply reproduces the areas of fast and slow change and, whenever these areas are distinguishable, the map is qualified as useful. The second criterion is the correct description of the map evolution over time. We proved the fulfilment of both criteria in the presence of environmental noise. We determined by the simulation the standard deviation of the phase noise above which the information in the map was destroyed. We showed that the phase noise impact was decreasing if this noise was time correlated. We found the normalized estimate for processing images acquired under non-uniform illumination with low sensitivity to ambient light. In a set of drying experiments with a phase noise and ambient light, we obtained the activity map evolution similar to that observed for the GT maps.

In Chapter 3, we proposed and analysed usage of three methods for image compression in the DSA: JPEG/JPEG2000, SVD and PCA compression. Our analysis proved that compression works well for symmetric/asymmetric speckle intensity distributions and can be used for images acquired at non-uniform illumination when normalized processing is required. How effective JPEG and JPEG2000 formats are for compressing dynamic speckle data is not a trivial question. On the one hand, the DSA is predominantly qualitative: it simply indicates areas with different speed of ongoing processes. The output is a 2D activity map, revealing regions on the object surface with fast or slow intensity changes, as well as the speed of the underlying process causing these variations. As we have proven by processing synthetic and experimental speckle data, both JPEG formats provide high quality of activity visualization at comparatively high compression ratios, e.g. 50 times decrease of storage size for colour images. On the other hand, the DSA has a potential for quantitative characterization provided some calibration procedure is introduced. Being transform based approaches, JPEG and JPEG2000 change the temporal correlation between the intensity values at a point to the extent, which depends on the compression ratio. This inevitably changes the functional dependence of the estimate statistics on time when observing a certain process. We limited our analysis of this issue to evaluating the change inflicted by compression on the average value of the activity estimate for a drying droplet of a polymer solution. We observed change in the time-dependence of the average with respect to the result for the bmp images, but this change was rather small. Given the significant gain in computer memory provided by the JPEG or JPEG2000 compression, our assessment is that distortion of time dependencies is of secondary importance. Therefore, recording the input data in the JPEG formats when carrying out measurements under outdoor conditions is feasible and guarantees reliable characterization of the observed dynamic events.

Next, we proposed two ways to apply SVD for compression and verified them for synthetic and experimental images. The first one decomposes the recorded speckle images, and the second one decomposes the arrays containing the difference between the intensity values in consecutive images. The first approach requires a larger number of nonzero singular values but it provides better spatial resolution in building the activity map. The second approach provides high quality of the activity map at smaller number of non-zero singular values, and compression substantially increases. The SVD method is suitable also for non-uniform illumination with normalized processing.

Further, we proposed a novel PCA-based lossy compression algorithm for DSA. The temporal correlation between the captured images enables applying a PCA approach for compression. Specificity of this compression scheme is that it is applied simultaneously to the whole set of speckle images used to compute the activity map whereas in the other proposed methods each image is compressed separately from the others. Compression is achieved by quantization and additional usage of autoencoders. The main drawback of the proposed approach is that it is computationally expensive. For instance, to compress single speckle image with JPEG standard, it takes 1.8 ms, while total encoding and decoding time for PCA-CH and PCA-CA algorithms it takes 1.1 s and 4.3 s respectively.

Next. we discussed new technologies for DSI application in non-destructive testing field.

We proposed and developed a portable low-cost set-up for outdoor implementation of the dynamic speckle technique. This set-up was realized on the base of a smartphone and demonstrated good stability in the presence of the environmental noise. The raw data were collected in the compressed data format. The set-up enables switching from laboratory to field conditions, substantially reduces price of the measurement and makes the DSI a versatile and easily accessible tool for users. In our research, we developed a laser device which was attached to the smartphone’s case and carried out sets of experiments. As GT data, we considered speckle images captured in laboratory environment with high-end equipment and the built from them activity maps. For the low-cost setup, we used Xiaomi Mi 9T and a self-developed laser device to capture speckle images. The smartphone was connected to PC as i) IP-camera and ii) USB-camera. In the last experiment, speckle images were captured and stored in the smartphone’s memory. We repeated each experiment twice at different image resolution: 1920×1080 and 3840×2160. Xiaomi Mi 9T was used as IP and USB camera by applying iVCam software. This software reduced quality of the speckle images and, hence, of the activity maps since the images were transferred being compressed with JPEG standard at low quality level. Best quality was achieved in the last set of experiments when the speckle images were captured and stored in the smartphone’s memory. In addition, such type of data capture is the fastest between the three types of connection which makes it suitable for detection of fast changing processes.

As a next task, we implemented the DSI technique with a high-speed camera for checking its potential for characterization of high strain rate events as e.g. high speed impact testing of composites. We proved that the option of computing the activity map from only two speckle images provided reliable results and used such algorithms for statistical characterization of intensity variation due to the sample deformation. The DSI visualizes the changes which occur before and after the impact, waves of activity or periodic variation of the mean intensity in time. The results obtained with plates of different composite materials indicate change of speckle statistics during the measurement. The activity maps represent a differential characterization of the deformation. Their summation may give some description of the cumulative effect of the impact.

Finally, we proved that it is possible to use dynamic speckle for hidden defect detection. We proposed excitation of this speckle by subjecting the sample to tensile loading. We estimated stretching process of a rubber sample with a hidden defect by tension machine. The laser speckle photometry with this type of excitation shows high sensitivity even at small tensile speeds. Defects can be recognized as higher activity areas in activity maps.

Author contributions in the dissertation work

The primary original contributions of the dissertation lie in the applied-theoretical domain and serve as the foundation for developing and optimizing dynamic speckle imaging as a field within coherent optical metrology, contributing to the physics of wave processes. As a result of a systematic theoretical and experimental study, new solutions for advanced data processing and storage were proposed, and novel implementations of dynamic speckle imaging methods were developed. The main contributions of the results obtained in this dissertation are as follows:

1. Analysis of normalized algorithms for processing data with spatially varying speckle statistics, such as speckle images acquired under non-uniform illumination, is performed and the best options are indicated [A1]. Methods for improving temporal resolution in pointwise dynamic speckle imaging are proposed by analysing impact of the acquisition time on quality of the 2D activity map as the measurement output [A2]. An intensity - based algorithm is developed for tracking fast changing processes with high temporal resolution [A3].
2. Analysis of the environmental noise as vibration induced phase fluctuations and shot noise from ambient light is performed and feasibility of the outdoor dynamic speckle measurements is confirmed [A4, A5].
3. For the first time, lossy compression schemes for disk storage optimization of temporally correlated speckle images using JPEG and JPEG2000 formats [A6] and two SVD-based compression algorithms [A7] are proposed and verified both by simulation and experiment. For the first time, a novel PCA-based temporal compression algorithm for lossy compression of a set of speckle images, that outperforms the JPEG compression results in preserving quality of the activity map, is developed.
4. In the field of non-destructive testing, a novel miniature portable device, based on a low - cost laser attached to a smartphone, was built and its efficiency was proved under field conditions [A8]. The dynamic speckle imaging potential in impact testing with a high - speed camera is studied [A9] and visualization of the deformation process is shown. Hidden defect detection by dynamic speckle excitation under tensile loading is proposed and verified [A10].

Literature

[1] J. W. Goodman, Statistical properties of laser speckle patterns, Laser speckle and related phenomena (pp. 9-75): Berlin, Heidelberg: Springer Berlin Heidelberg., 1975.

[2] Mininni, M., Gabriele, S., Lopes, H., & dos Santos, J. A, "Damage identification in beams using speckle shearography and an optimal spatial sampling," *Mechanical Systems and Signal Processing, 79,* pp. 47-64, 2016.

[3] Edwards, T. E. J., Di Gioacchino, F., Springbett, H. P., Oliver, R. A., & Clegg, W. J., "Stable speckle patterns for nano-scale strain mapping up to 700 C," Experimental mechanics, 57, pp. 1469-1482, 2017.

[4] Jaideva C. Goswami, Andrew K. Chan, Fundamentals of Wavelets: Theory, Algorithms and Applications, New York: Wiley-Interscience 1999, 1999.

[5] H. Fujii, "Blood flow observed by time-varying laser speckle," Opt. Letters 10(3), pp. pp. 104-106, 1985.

[6] R. Arizaga, N. Cap, H. Rabal, M. Trivi, "Display of the local activity using dynamical speckle patterns," Opt. Engg. 41(2), pp. pp. 287-294, 2002.

[7] A. V. Saude, F. S. de Menezes, P. L. S. Freitas, G. F. Rabelo and R. A. Braga, "Alternative measures for biospeckle image analysis," J. of Opt. Society of Am.A 29(8), pp. pp. 1648-1658, 2012.

[8] Stoykova, E., Ivanov, B., & Nikova, T., "Correlation-based pointwise processing of dynamic speckle patterns," Opt. Lett. 39(1), pp. 115-118, 2014.

[9] Stoykova E, Nazarova D, Berberova N and Gotchev A, "Performance of intensity-based non-normalized pointwise algorithms in dynamic speckle analysis," Optics Express, 23(19), pp. 25128-25142., 2015.

[10] Asakura, T., & Takai, N., "Dynamic laser speckles and their application to velocity measurements of the diffuse object," *Applied physics, 25,* pp. 179-194, 1981.

[11] Briers, J. D., "Speckle fluctuations and biomedical optics: implications and applications," *Optical Engineering, 32(2),* pp. 277-283, 1993.

[12] H. Fujii, K. Nohira, Y. Yamamoto, H. Ikawa, and T. Ohura, "“Evaluation of blood flow by laser speckle imaging sensing Part I," *Appl. Opt. 26(24),* p. 5321–5325, 1987.

[13] Lasser, T, Serov, A., "High-speed laser Doppler perfusion," *Opt. Express,* p. 6416–6428, 2005.

[14] Stoykova, E., Blagoeva, B., Nazarova, D., Nedelchev, L., Nikova, T., Berberova, N., ... & Kang, H. J. , "“Evaluation of temporal scales of migration of cosmetic ingredients into the human skin by two-dimensional dynamic speckle analysis," *Opt. Quant.Electron. 50,* pp. 191-201, 2018.

[15] A. Chatterjee, P. Singh, V. Bhatia, and S. Prakash, "“Ear biometrics recognition using laser biospeckled fringe projection profilometry," *Opt. Las. Technol. 112,* pp. 368-378, 2019.

[16] S. E. Murialdo, G. H. Sendra, L. I. Passoni, R. Arizaga, J. F., "Analysis of bacterial chemotactic response using dynamic laser speckle," *J. Biomed. Opt. 14(6),* p. 064015, 2009.

[17] B. Mandracchia, J. Palpacuer, F. Nazzaro, V. Bianco, R. Rega, and P. Ferraro, "“Biospeckle decorrelation quantifies the performance of alginate-encapsulated probiotic bacteria," *IEEE Journal of Selected Topics in Quantum Electronics 25(1),* pp. 1-6, 2018.

[18] R. A. Braga, L. Dupuy, M. Pasqual, and R. R. Cardoso, "Live biospeckle laser imaging of root tissues," *Eur. Biophys. J. 38(5),* p. 679–686, 2009.

[19] B. Ivanov, E. Stoykova, N. Berberova, T.Nikova, E. Krumov, and N. Malinowski, "Dynamic speckle technique as a leaf contamination sensor," *Bulg. Chem. Commun. 45(3),* p. 149 – 153, 2013.

[20] R. Braga, I. Fabbro, F. Borem, G. Rabelo, R. Arizaga, H. Rabal, and M.Trivi, "Assessment of seed viability by laser speckle technique," *Biosystems Eng. 86(3),* pp. 287-294, 2003.

[21] R. Macedo, J. Barreto Filho, R. Braga, Jr, and G. Rabelo, "Sperm motility decreasing and semen fertility in the bull evaluated by biospeckle," *Reprod. Fertil. Dev. 22,* p. 170–171, 2009.

[22] M. Z. Ansari, P. D. Minz, and A. K. Nirala, "Fruit quality evaluation using biospeckle techniques," *IEEE,* p. 873–876, 2012.

[23] C. Mulone, N. Budini, F. Vincitorio, C. Freyre, A. López Díaz, and A. Ramil Rego, "Analysis of strawberry ripening by dynamic speckle measurments," *Proc. SPIE 8785,* p. 87851, 2013.

[24] T. Lyubenova, E. Stoykova, E. Nacheva, B. Ivanov, I. Panchev, and V. Sainov, "Monitoring of bread cooling by statistical analysis of laser speckle patterns," *SPIE 8770,* p. 87700S, 2013.

[25] R. Harizanova, V. Gaydarov, G. Zamfirova, E. Stoykova, D. Nazarova, B. Blagoeva, and L. Nedelchev, "Probing of the mechanical properties and monitoring of the drying process of azopolymer thin films for optical recording," *Thin Solid Films 687,* p. 137441, 2019.

[26] L. Martí-López, H. Cabrera, R. A Martínez-Celorio, and R. González-Peña, "Temporal difference method for processing dynamic speckle patterns," *Optics Communications 283(24),* pp. 4972-4977, 2010.

[27] Hu, Y. J., Wang, Y. J., Chen, J. B., & Zhu, J. M., "A new method of creating high-temperature speckle patterns and its application in the determination of the high-temperature mechanical properties of metals," *Experimental Techniques,* vol. 42, pp. 523-532, 2018.

[28] Kayahan, E., Oktem, H., Hacizade, F., Nasibov, H., & Gundogdu, O., "Measurement of surface roughness of metals using binary speckle image analysis," *Tribology International,* Vols. 43(1-2), pp. 307-311, 2010.

[29] Qu, Z., Fang, X., Hou, G., Su, H., Feng, X., Li, H., ... & Fukuta, Y, "Ceramic-based speckles and enhanced feature-detecting algorithm for deformation measurement at high temperature," *Experimental Mechanics,* vol. 57, pp. 377-386, 2017.

[30] Chen, L., Cikalova, U., & Bendjus, B., "Laser speckle photometry: an advanced method for defect detection in ceramics," *In Speckle 2018: VII International Conference on Speckle Metrology,* vol. 10834, pp. 302-308, 2018, September.

[31] Zimnyakov, D., Alonova, M., Ushakova, E., Volchkov, S., Ushakova, O., Klimov, D., ... & Kalacheva, A., "Speckle-based sensing of microscopic dynamics in expanding polymer foams: Application of the stacked speckle history technique," *Sensors,* vol. 21(20), p. 6701, 2021.

[32] Nazarchuk, Z. T., Muravsky, L. I., & Kuts, O. G., "Nondestructive testing of thin composite structures for subsurface defects detection using dynamic laser speckles," *Research in Nondestructive Evaluation,* vol. 33(2), pp. 59-77, 2022.

List of publications

A1. Stoykova, E., Nazarova, D., Nedelchev, L., **Levchenko, M.**, Berberova-Buhova, N., Ivanov, B., Normalization in dynamic speckle analysis for non-destructive monitoring of speed of processes, Journal of Physics: Conference Series, 2091 (1), art. no. 012002, DOI: 10.1088/1742-6596/2091/1/012002, (2021)

A2. **Levchenko, M**, Stoykova E., Madjarova V. Temporal resolution improvement in dynamic speckle analysis. Journal of International Scientific Publications: Materials, Methods & Technologies 16, 189-197 (2022)

A3. Stoykova, E., Nedelchev, L., Blagoeva, B., Ivanov, B., **Levchenko, M.**, Berberova-Buhova, N., Nazarova, D., Intensity based dynamic speckle method for analysis of variable-rate dynamic events, Proceedings of SPIE, 12618, art. no. 1261829, DOI: 10.1117/12.2673462, (2023)

A4. **Levchenko, M**., Stoykova, E., Ivanov, B., Nedelchev, L., Nazarova, D., Choi, K., & Park, J. Noise analysis in outdoor dynamic speckle measurement. Applied Optics, 62(10), D187-D195. (2023)

A5. Stoykova, E., **Levchenko, M.**, Blagoeva, B., Nazarova, D., Nedelchev, L., Berberova-Buhova, N., Choi, K., Park, J., Environmental Noise Impact on Dynamic Speckle Imaging, Optics InfoBase Conference Papers, art. no. W1A.3, (2022)

A6. Stoykova, E., Blagoeva, B., Berberova-Buhova, N., **Levchenko, M.**, Nazarova, D., Nedelchev, L., Park, J., Intensity-based dynamic speckle method using JPEG and JPEG2000 compression, Applied Optics, 61 (5), pp. B287-B296, DOI: 10.1364/ AO.444831, (2022)

A7. Stoykova, E., **Levchenko, M.**, Ivanov, B., Madjarova, V., Nazarova, D., Nedelchev, L., Machikhin, A., Park, J., Dynamic speckle imaging with SVD compression, Journal of Physics: Conference Series, 2407 (1), art. no. 012049, DOI: 10.1088/1742-6596/2407/1/012049, (2022)

A8. **Levchenko, M**., Stoykova, E., Hong, K., Park, J., Portable low-cost set-up for outdoor implementation of dynamic speckle technique, Proceedings of SPIE, 12618, art. no. 126181I, DOI: 10.1117/12.2673460, (2023)

A9. **Levchenko M.**, Anisimov A., Stoykova E. (2024) Speckle techniques with a high-speed camera for deformation evaluation of composites during impact testing. HISTRATE conference on Advanced Composites under High Strain Rates Loading: A Route to Certification-by-Analysis, Istanbul, June 5-6, 2024

A10. Stoykova E., **Levchenko M.**, Ivanov B., Nazarova D (2024) Hidden defects detection under tensile loading by laser speckle photometry. HISTRATE conference on Advanced Composites under High Strain Rates Loading: A Route to Certification-by-Analysis, Istanbul, June 5-6, 2024

List of presentations

Oral presentations

B1. Fifth International Conference on Applications of Optics and Photonics, Guimarães, Portugal 17 – 22 July 2022
B2. Digital Holography and 3-D Imaging, Cambridge United Kingdom, 1–4 August 2022
B3. SPIE Optical Metrology 2023 conference, Munich, Germany, 26 - 29 June 2023
B4. HISTRATE conference on Advanced Composites under High Strain Rates Loading: A Route to Certification-by-Analysis, Istanbul, June 5-6, 2024
B5. Bulgarian-Korean Workshop, Photonics and Sensorics, Sofia, Bulgaria, 10 – 11 October 2024

Poster sessions

B6. International Scientific Publications, Materials, Methods & Technologies, Burgas, Bulgaria, 29 August, 2022
B7. SPIE Optical Metrology 2023 conference, 26 - 29 June 2023, Munich, Germany
B8. HISTRATE conference on Advanced Composites under High Strain Rates Loading: A Route to Certification-by-Analysis, Istanbul, June 5-6, 2024

List of citations

Paper

Stoykova, E., Blagoeva, B., Berberova-Buhova, N., **Levchenko, M.**, Nazarova, D., Nedelchev, L., Park, J., Intensity-based dynamic speckle method using JPEG and JPEG2000 compression, Applied Optics, 61 (5), pp. B287-B296, DOI: 10.1364/ AO.444831, (2022)

Cited in

1. Ghadami, R., & Rahebi, J. Compression of images with a mathematical approach based on sine and cosine equations and vector quantization (VQ). Soft Computing, 27(22), 17291-17311. (2023)
2. Rubio-Oliver, R., Sanz, M., Sigalov, M., García, J., & Beiderman, Y. Spatially Multiplexed Speckle on 1D Sensors for High-Speed 2D Sensing Applications. Sensors, 24(11), 3293. (2024)

Paper

Stoykova, E., **Levchenko, M.**, Ivanov, B., Madjarova, V., Nazarova, D., Nedelchev, L., Machikhin, A., Park, J., Dynamic speckle imaging with SVD compression, Journal of Physics: Conference Series, 2407 (1), art. no. 012049, DOI: 10.1088/1742-6596/2407/1/012049, (2022)

Cited in

1. Temeemy, A. A. ALI: The adaptive levels of interval method for processing laser speckle images with superior activity extraction and discrimination capabilities. Optics and Lasers in Engineering, 178, 108173. (2024)

Paper

Levchenko, M., Stoykova, E., Hong, K., Park, J., Portable low-cost set-up for outdoor implementation of dynamic speckle technique, Proceedings of SPIE, 12618, art. no. 126181I, DOI: 10.1117/12.2673460, (2023)

Cited in

1. Rubio-Oliver, R., Sanz, M., Sigalov, M., García, J., & Beiderman, Y. Spatially Multiplexed Speckle on 1D Sensors for High-Speed 2D Sensing Applications. Sensors, 24(11), 3293. (2024)

Acknowledgments

This doctoral dissertation has been prepared within the European Joint Doctoral Programme on Plenoptic Imaging (PLENOPTIMA) and received funding from the European Union’s Horizon 2020 research and innovation programme under the Marie Skłodowska-Curie grant agreement No 956770.